THESIS

ESTIMATING SPARSE INVERSE COVARIANCE MATRIX FOR BRAIN COMPUTER INTERFACE APPLICATIONS

Submitted by

Annamalai Natarajan

Department of Computer Science

In partial fulfillment of the requirements

for the Degree of Master of Science

Colorado State University

Fort Collins, Colorado

Fall 2009

COLORADO STATE UNIVERSITY

October 9, 2009

WE HEREBY RECOMMEND THAT THE THESIS PREPARED UNDER OUR SUPERVISION BY ANNAMALAI NATARAJAN ENTITLED ESTIMATING SPARSE INVERSE COVARIANCE MATRIX FOR BRAIN COMPUTER INTERFACE APPLICATIONS BE ACCEPTED AS FULFILLING IN PART REQUIREMENTS FOR THE DEGREE OF MASTER OF SCIENCE.

Committee on Graduate Work

Committee Member

Committee Member

Advisor

Co-Advisor

Acting Department Chair

ABSTRACT OF THESIS

ESTIMATING SPARSE INVERSE COVARIANCE MATRIX FOR BRAIN COMPUTER INTERFACE APPLICATIONS

In this project we present a brain-computer interface (BCI) which recognizes one task from another in a timely manner. We use quadratic discriminant analysis to classify Electroencephalography (EEG) samples in an online fashion. The raw EEG samples are collected over half second intervals to estimate the power spectral densities. The estimated power spectral densities are treated as individual samples by the classifier. The mean and inverse covariance matrix parameters in the classifier are updated incrementally as samples arrive spread over several training sessions. We also perform some feature selection using only descriptive statistics of the collected data to throw away irrelevant and redundant features. We have constrained the tasks to be imagination of actual tasks to ready the BCI for real world applications. We evaluated the performance of the BCI on two experiments. In experiment I the BCI achieves a moderate 74% classification accuracy when recognizing a right hand task from a visual spinning task. In experiment II it achieves a poor performance of 57% when classifying a right hand task from left foot.

Annamalai Natarajan
Department of Computer Science
Colorado State University
Fort Collins, CO 80523
Fall 2009

ACKNOWLEDGMENTS

I would like to thank my advisor, Dr. Charles Anderson, for his constant support and guidance rendered during this thesis work. Special thanks to Dr. Patricia Davies for showing me a different perspective of the human brain. I am grateful to Dr. Michael Kirby for serving on my committee. I would like to thank Dr. William Gavin for many fruitful discussions. I would also like to thank Asbjørn Berge, Are C. Jensen, and Anne H. Schistad Solberg for their help with the incremental QDA algorithm. Lastly I would like to thank my friends and family for their support.

TABLE OF CONTENTS

LIST OF FIGURES

LIST OF TABLES

Chapter 1

Introduction

A human machine interface serves as a medium of communication between humans and external devices. The brain-computer interface is a form of human machine interface that helps connect the brain to external devices. The connection is typically via a computer system to process, infer and translate users' intentions into actions. Wolpaw, et al., define BCI as a communication system that does not depend on the brain's normal output pathways of peripheral nerves and muscles [1]. BCI's in offline mode operate in two phases: training and testing. In the training phase the subjects perform different tasks (imagine moving hands, feet, doing simple math, etc) and the BCI is trained to recognize one task from another. In the testing phase the already trained BCI is tested on new data for their generalization capability and performance. Besides numerous challenges like the quality of Electroencephalography (EEG) signals (its non-stationary nature, neurons firing property, convoluted cerebral cortex, all explained in Chapter 2), common EEG artifacts [2] and also the underlying brain activity in actual and imagery tasks, the BCI still qualifies as a medium of communication for subjects with locked in syndrome. BCI's are pursued with active interest in subjects with amyotrophic lateral sclerosis (ALS), stroke, high level spinal cord injury, cerebral palsy or amputation. They could also assist or aid in identification of human cognitive and sensory motor functions.

BCI's equipped with EEG for data collection are easy to setup, can be deployed

in numerous environments, are preferred for their lack of risk and are inexpensive. Other techniques used to map brain activation are functional magnetic resonance imaging (fMRI), positron emission tomography (PET) and magnetoencephalography (MEG). fMRI measures the changes in blood flow level (blood oxygen level dependent (BOLD) level) in the brain. In PET a tracer isotope is injected into the subject that emits gamma rays when it annihilates, these gamma rays are further traced by placing the subject under a scanner. These approaches have relatively poor time resolution but excellent space resolution when compared to EEG. MEG is an imaging technique that measures the magnetic fields produced by electrical activity; EEG can be simultaneously recorded along with MEG.

Clearly, from the description above, it can be noted that the BCI is a classification problem. It will need to recognize one task from another for it to function efficiently. In artificial intelligence (AI), machine learning approaches are broadly classified into supervised, unsupervised and reinforcement learning. In supervised learning the training data is accompanied by target vectors, in unsupervised learning no target vectors are provided; the goal is to group the training data into clusters. Reinforcement learning is finding suitable actions in environments to maximize rewards. In our approach we use supervised learning to train the BCI with training fraction samples and associated target vectors and then test for its generalization capability. No matter what the learning approach is, the choice of an appropriate algorithm plays a crucial role. Factors like algorithm complexity, computational complexity, number of parameters, ease of implementation and memory requirements determine the choice of algorithms. Several machine learning algorithms, in no particular order, like discriminant analysis, support vector machines (SVM), hidden markov models (HMM), multilayer perceptrons, Bayes classifier, principal component analysis (PCA), independent component analysis (ICA), K nearest neighbors (kNN), common spatial pattern (CSP) and expectation maximiza-

tion (EM) have enjoyed success in BCI applications.

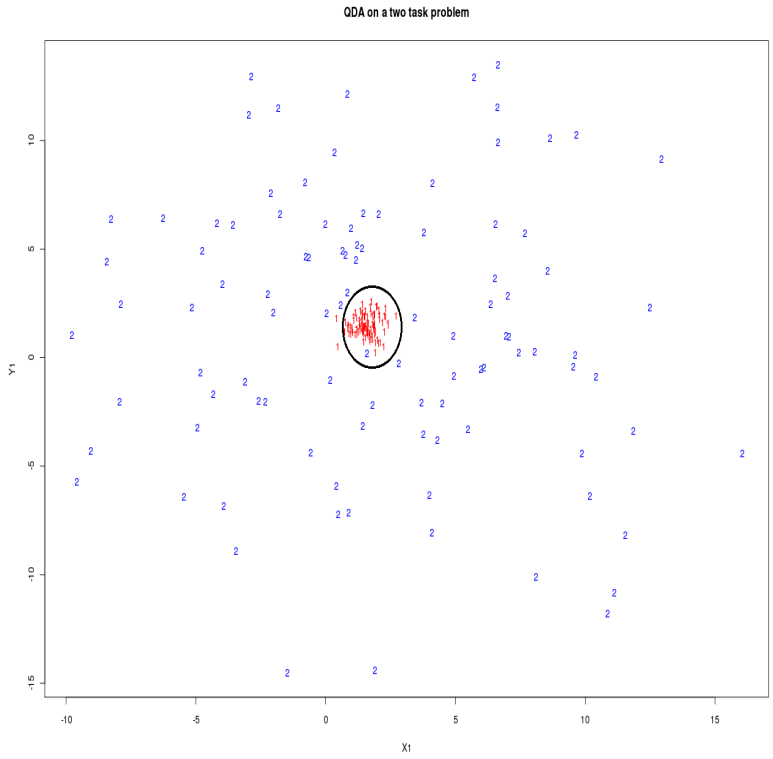

Figure 1.1: Discriminant analysis

In our approach we have implemented a variation of discriminant analysis called the quadratic discriminant analysis (QDA). The general idea of discriminant analysis is to find a combination of features that best discriminates one task from another. Figure 1.1 captures the idea of discriminant analysis in a two class problem. Class 1 is concentrated in the center and class two is scattered around. The circle serves as the discriminatory function; any sample falling inside the circle belongs to class 1 otherwise it belongs to class 2. In QDA the combination of features is quadratic. The basic assumption in QDA is that the data from each each class is normally distributed. It computes two parameters per task, the mean and the covariance, from the train data using them in a discriminant function to determine the target class. The limits of this approach are its generalization

capability and the time taken to compute the parameters. It takes a fairly large time for large datasets. Considering the QDA for a BCI application, where subsequent training sessions have been demonstrated to be successful [3, 4, 5], it would be more efficient if the parameters could be updated in subsequent sessions rather then computing it from scratch; this will also prove to be time saving in real world deployment. This is precisely the idea behind incremental QDA where we estimate the parameters rather than computing them. From pilot experiments it appears that the estimated parameters are close to the computed parameters when the number of samples is large. In terms of performance the regular (using computed parameters) and incremental (using estimated parameters) approaches converge. In addition to estimating the parameters we also perform some feature selection to improve the recognition rates as not all features are likely to contribute to recognition of all the tasks.

The objectives of this project are summarized under two hypothesis below,

Hypothesis I

- Experiment with an incremental way to update mean and inverse covariance parameters
- The recognition rates of the incremental QDA should be comparable or better than batch QDA (parameters are computed)
- The incremental QDA approach should be time efficient

Hypothesis II

- Feature Selection should improve the BCI performance significantly
- Feature Selection Should also minimize the number of parameters (i.e. inverse covariance matrix entries thereby making it sparse) to be estimated

The rest of this report is organized as follows. Chapter 2 gives a brief overview of the human brain and associated activities. Chapter 3 outlines the brain-computer interface architecture and explains each component in detail. Chapter 4 evaluates the performance of the BCI. Chapter 5 concludes this report and highlights the directions on future work.

Chapter 2

Background

This chapter is a brief introduction to the human brain from a neuroscience perspective. We also outline the source of EEG activity and give an overview of BCI models.

The human brain is the site of consciousness, allowing humans to think, learn and create. The brain is broadly divided into the cerebrum, cerebellum, limbic system and the brain stem. The cerebrum is covered with a symmetric convoluted cortex with a left and right hemispheres. The brain stem is located below the cerebrum and the cerebellum is located beneath the cerebrum and behind the brain stem. The limbic system which lies at the core of the brain contains the thalamus and hypothalamus among other parts. Anatomists divide the cerebrum into Frontal, Parietal, Temporal and Occipital lobes. These lobes inherit their names from the bones of the skull that overlie them. It is generally agreed that the Frontal lobe is associated with planning, problem solving, reasoning, parts of speech, bodily movement and coordination. The Parietal lobe is associated with bodily movement, orientation and recognition (such as touch, taste, pressure, pain, heat, cold, etc). The Temporal lobe is associated with perception, auditory stimuli, memory and speech. The Occipital lobe is associated with visual stimuli. Figure 2.1 is an image of human brain with the lobes and their associated functions.

The brain is made up of approximately 100 billion neurons. Neurons are nerve cells with dendrite and axon projections that take information to and from the nerve

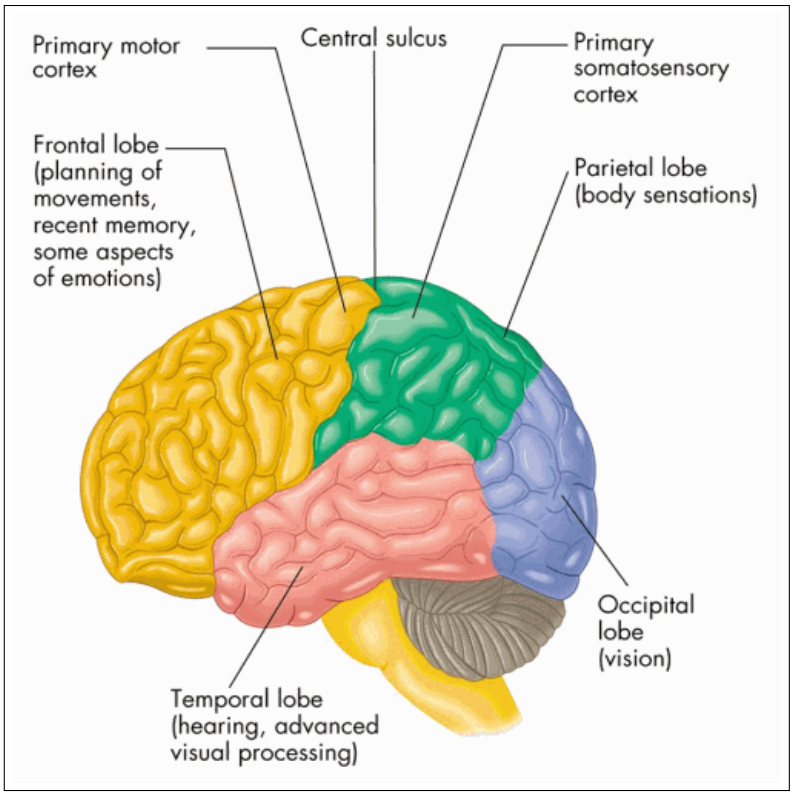

Figure 2.1: The human brain [6]

cells, respectively. These neurons have a resting potential, typically between -70 to -65 microvolts, which is the difference between the interior potential of the cell and the extra cellular space. A stimulus triggers an action potential in the neuron which sends out information (also know as firing property, impulse, spike) along the axons. Neurons transmit messages electrochemically. A neuron fires only when its resting potential drops below a threshold of -55 microvolts. A spiking neuron triggers another neuron to spike and in turn another. This causes the resting potential to fluctuate as a result of impulses arriving from other neurons at contact points (synapses). These impulses result in post synaptic potentials which cause electric current to flow along the membrane of the cell body and dendrites. This is the source of brain electric current. Brain electrical current consists mostly of Na+, K+, Ca++, and Cl- ions. Only large populations of

active neurons can generate electrical activity strong enough to be detected at the scalp as neurons tend to line up to fire. The Electroencephalogram is defined as electrical activity of an alternating type recorded from the scalp surface after being picked up by metal electrodes and conductive media [7]. Electroencephalography (EEG) is the process of picking up the electrical activity from the cortex. Hans Berger suggested that periodic fluctuations of the EEG might be related in humans to cognitive processes [8]. Electrical activity recorded of the scalp with surface electrodes constitute a non-invasive approach to gathering EEG data, while semi-invasive or invasive approaches implant electrodes under the skull or on the brain, respectively [9]. The trade off in these approaches lies in the EEG source localization, quality of EEG data, surgical process involved and/or the effect of the electrodes interacting with the tissues.

EEG recorded over a continuous period of time are characterized as spontaneous EEG. These signals are not time locked and are usually triggered by an auditory or visual cue. Another closely related application of EEG is the event related potential. Electrical activity triggered by presenting a stimulus is time locked and is an evoked response. These evoked responses are called the event related potentials (ERP). The latency and peaks in the evoked responses are in predictable ranges given the stimulus. Typically ERP's are recorded from a single electrode over the region of activation along with a ground electrode. EEG has applications among clinical diagnosis, neuroscience and the entertainment (gaming) industry.

EEG activity is broadly divided into five frequency bands. The boundaries are flexible but do not vary much from 0.5-4 Hz (delta), 5-8 Hz (theta), 9-12 Hz (alpha), 13-30 Hz (beta) and above 30 Hz (gamma) frequencies. Refer to Figure 2.2 for EEG frequency bands. The EEG frequencies and their associated activities are the delta activity is associated with deep sleep. Theta activity is associated with hypnagogic imagery, rapid eye movement (REM), sleep, problem solving, attention and hypnosis [8]. Alpha activity is

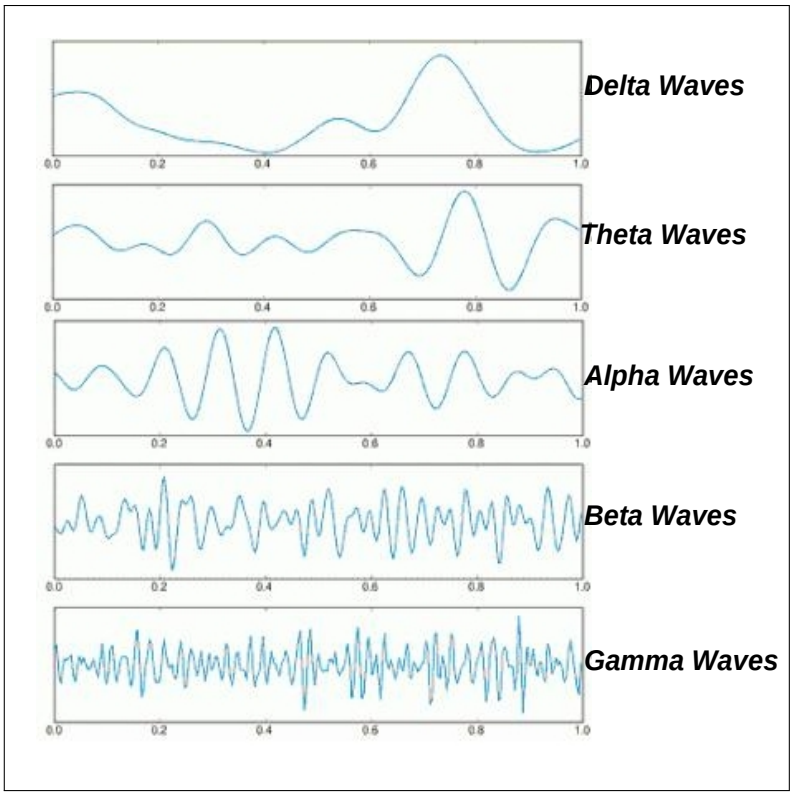

Figure 2.2: EEG frequencies [10]

associated with relaxation and non-cognitive processes [11]. Beta activity with active thinking or active attention [11]. Gamma frequencies are associated with attention and recognition [12].

Over the years various BCI models have been developed which categorically fall into the BCI model spectrum. The primary difference lies in the interaction between the user and the BCI. At one end of the BCI model spectrum is an architecture where all emphasis is placed on the subject to generate quality EEG data with little effort on the BCI to recognize the task. In a way it is training the subject to control their EEG activity. On the other end of the spectrum the burden lies on the BCI to recognize the task with the user putting in little effort to generate quality data. Somewhere in between this spectrum is an architecture where both the subject and the BCI mutually learn and

evolve together. This is achieved when the BCI gives feedback to the user regarding the quality of EEG data generated [9]. Some BCI architectures also use the error related negativity (ERN) signals, a type of ERP, which are used along with the EEG to aid in identification of the subject's true intentions [13].

Chapter 3

Methods

This chapter provides details on the brain-computer interface model. Section 3.1 presents the BCI architecture and the flow of control in this BCI model. Section 3.2 describes the experimental setup and procedures followed in the lab when collecting EEG data, Section 3.3 gives details of the dataset used in the experiments, Section 3.4 explains the Welch periodogram approach to estimate the power spectral densities from raw EEG data. Section 3.5 outlines the theory and math in the incremental QDA classifier algorithm. Section 3.6 evaluates how close the estimated parameters are to the computed ones. Section 3.7 details on feature selection and the associated preprocessing.

3.1 Brain Computer Interface Architecture

Our brain-computer interface model is geared towards an online approach where timely, reliable response is of paramount importance. We adopt a non-invasive method to gather brain electrical activity from the scalp electrodes. The subject is instructed to imagine performing different tasks. The EEG data, typically in microvolts, is amplified then converted to digital signals before being processed. The BCI architecture used in this project is outlined in Figure 3.1.

In the offline mode EEG data samples are divided into train, validation and test par-

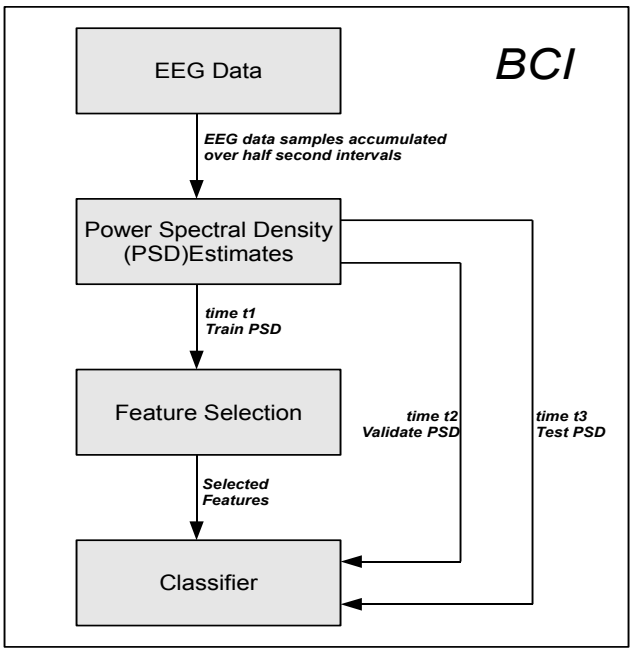

Figure 3.1: The Brain Computer Interface architecture

titions. Within each partition the samples are collected over half second windows to estimate the power spectral densities. Power spectral density (PSD) gives the distribution of average power with respect to the frequencies in the EEG signal. The estimated PSD's are binned and treated as individual features within each channel. At time $t1$ the incremental classifier is trained on these features and the feature selector also ranks these features. At time $t2$ the ranked features are evaluated on the validation partition to determine the bounds on the number of features that help in recognizing the tasks. At time $t3$ all features within the selected bounds are used on the test partition to evaluate the performance.

3.2 EEG Data

In our non-invasive approach the subject wears an electrode cap. The electrodes on the cap are placed as per the 10-20 system, refer to Figure 3.2. The electrodes on the right hemisphere are even numbered and to the left are odd numbered. The letters on the electrodes correspond to the lobes as explained in Chapter 2. In addition to the Frontal, Temporal, Parietal and Occipital lobes, two regions the pre-Frontal (a region in the frontal lobe) and Central (a region in between the frontal and parietal lobes) are included. Scalp recordings of neuronal activity in the brain allow measurement of potential changes over time in the basic electric circuit conducting between the signal (active) electrodes and reference electrodes [14]. In our setup the reference electrodes, A1 and A2, are placed on the left and right ear (preauricular points), respectively. Not shown in Figure 3.2 is the ground electrode which lies in the center of the Fp1, Fp2, FZ triangle which also pertains to our setup. We used a Mindset [15] EEG recorder to collect data.

A conductive gel is applied to bridge the gap between the scalp and the electrodes. Impedance at each scalp-electrode contact is adjusted to be less then 5 kilo-ohms in order to lower signal distortions (equipment dependent). This is done by twirling a wooden stick around in each channel until the impedances begin to drop covering all channels repeatedly. Subjects are instructed to perform imagination of actual tasks with a cue. We used the CEBL software [17] in which the order of tasks are randomly determined. The visual cues for each task appear for a specific time period interspersed with idle periods. The EEG signals recorded from the scalp are amplified, digitized and preprocessed for artifacts. Common artifacts include eye movement, muscle movement, electric motors, electric lights, etc. While standard lab procedures help eliminate most artifacts, some artifacts like eye blinks are inevitable. The CEBL software is equipped with a maximum noise fraction (MNF) filter to filter out the high and low frequencies [2]. Refer to Figure 3.3 for sample EEG data from 19 channels over a five second interval. Eye blink artifacts

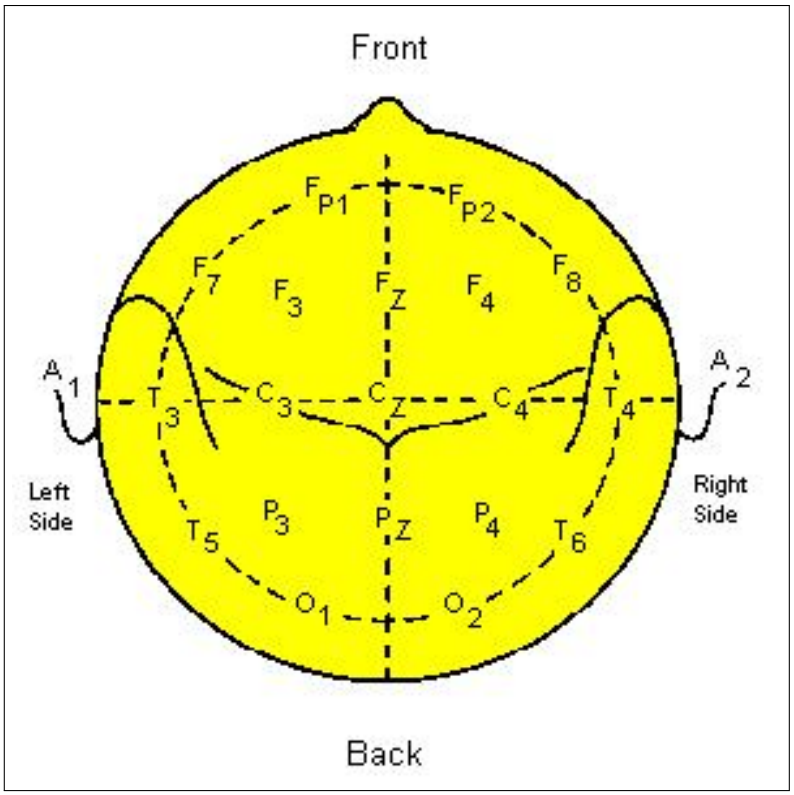

Figure 3.2: The 10-20 system of placement of electrodes [16]

can be spotted around one second in the frontal and pre-frontal channels.

All the experiments were performed on the same dataset. We collected data from a right handed male subject with no known medical history. The subject performed four imagined tasks based on a visual cue from the CEBL software [17]. The data was recorded on the same day in two recording sessions of ten sequences each with a ten minute interval between subsequent sessions. The four tasks were imagination of right hand movement, imagination of left leg movement, counting backwards from 100 by 3 and mental rotation of a three dimensional object. The sampling rate is set to 256 Hz on a Mindset [15] recorder. There are 20 sequences per task, each sequence lasts for about 4 to 5 seconds. We recorded data from 19 surface electrodes as shown in Figure 3.2. The data is not preprocessed for artifacts.

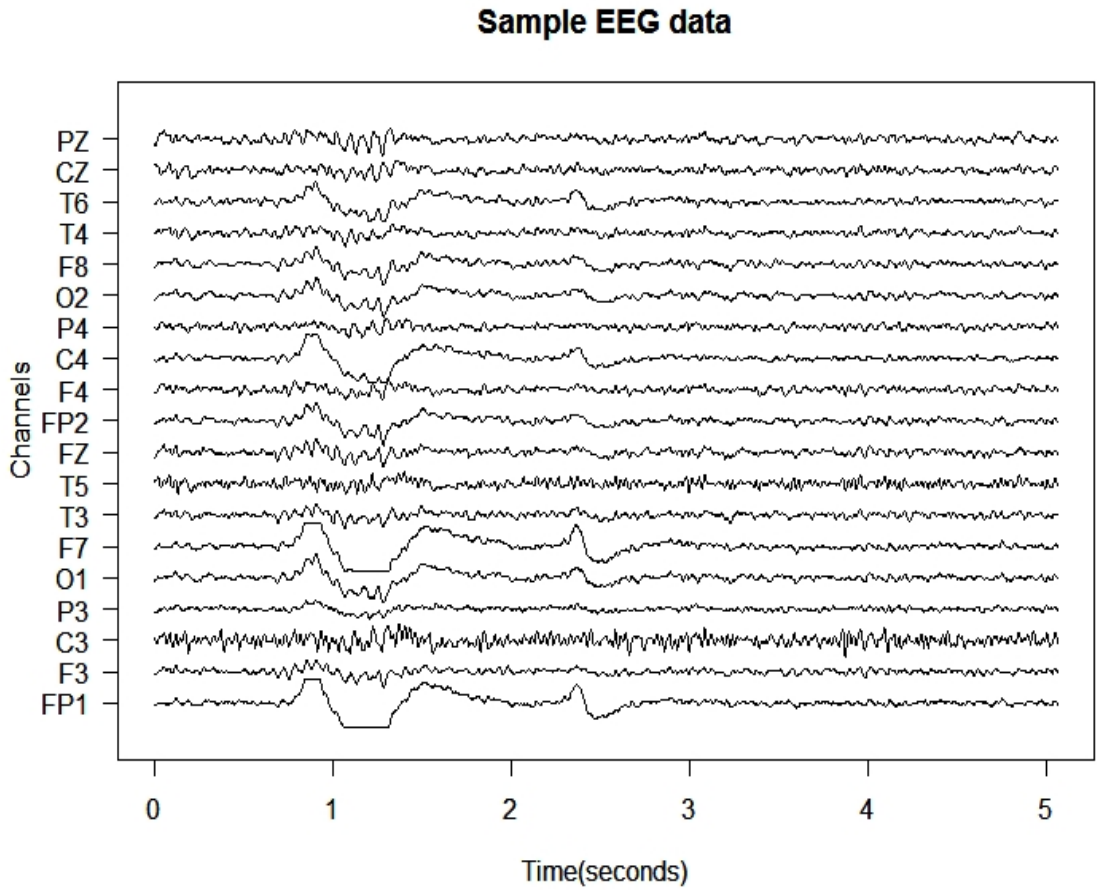

Figure 3.3: Sample EEG data from 19 channels

3.3 Power Spectral Density Estimation

The areas of activation in the brain vary with the tasks (classes) as do the associated EEG frequencies. For instance bodily movement causes the central and parietal lobe to generate EEG between 12 Hz (alpha) and 30 Hz (beta). Refer to Figure 2.2 for EEG frequencies. The power of any signal is defined as the energy per unit time of a signal. Hence the average power at the scalp electrodes along the direction of the firing neurons will be relatively high when compared to the power at the electrodes farther away from the line of firing neurons. The PSD's estimated from raw EEG data closely model

the underlying brain frequencies and also improve the classification accuracy [18, 19]. The power spectral density is an estimate of the signal's power falling within frequency ranges. To estimate the PSD's we will need to transform the time domain EEG data into frequency representations. The occurrence of the frequency components is independent of where in time this component appears. Therefore PSD estimates of stationary time signals is straightforward but in the case of EEG it is further complicated as the nonstationary nature of the human brain generates nonstationary EEG signals [20]. In order to represent the EEG signals in the frequency domain we would like to assume that the EEG signals are stationary over a short period of time. Valid assumptions tend to vary between 0.5 to a few seconds [21].

Two important parameters in estimating the power spectral densities are the upper and lower bound on the frequencies and how to group the frequencies. Several studies band pass filtered the frequency components between 6-30 Hz for imagery tasks. Pfurtscheller, et al., talks about three imagery tasks for patients with actual spinal cord injury; the frequencies were band pass filtered between 8-30 Hz [22]. Bin, et al., and Pfurtscheller, et al., band pass filtered between 6-30 Hz and 9-28 Hz, respectively, which covers both mu and beta rhythm for right and left hand imagery tasks [23, 24]. To group frequency components into bins we would like to know the active frequencies given the tasks. From the literature, Wolpaw, et al., showed that alpha (8-13Hz) and/or beta rhythm amplitudes could serve as effective inputs for a BCI to distinguish a movement or motor imagery task [25, 26]. Rescher and Rappelsberger performed data reduction of the spectra into five frequency bands as follows theta (4-7.5 Hz), alpha 1 (8-10 Hz), alpha 2 (10.5-12.5 Hz), beta 1 (13-18 Hz), beta 2 (18.5-24 Hz) [27]. Tanaka, et al., groups the frequencies in pairs (i.e., 6-7 Hz, 8-9 Hz) essentially a 2Hz resolution [19]. From pilot experiments with our dataset grouping the frequencies into 2 Hz bins increased the complexity by increasing the number of features and additionally our tasks did not

require this small a resolution in the sense we were expecting more changes at the alpha, beta frequency ranges. This led us to group the frequency components roughly based on the EEG frequency bands. Clearly this is another search problem that was not intended to be addressed as part of this thesis. We leave this for future work. One representation that works well for experiment I is frequency components that are band pass filtered between 6-24 Hz which covers the ranges for both tasks. The frequency components are grouped into five bins 6-7 Hz (theta), 8-10 Hz (alpha 1), 11-12 Hz (alpha 2), 13-20 Hz (beta 1) and 21-24 Hz (beta 2).

We use the Welch periodogram approach to estimate the PSD's (refer to the *Welch-PSDEstimates* pseudo code below). The *WelchPSDEstimates()* function takes as arguments the raw EEG data, the number of channels and the number of bins the frequency components will be grouped into. In addition the window type is set to a default Hanning window; the window size parameter specifies the time period over which the stationary property of the EEG is assumed to hold; the increment parameter (in percent) specifies by how many samples the window will need to shift. This last parameter could also be viewed as what percentage of the signal from the previous time window should be used to compute the frequency components in the current time window.

WELCHPSDESTIMATES$(EEGdata, Channel, Bins)$

```
1  Window ← Hanning
2  WindowSize ← (No.ofsamplesPerHalfSecond)/2
       // WindowSize: EEG data accumulated over half second intervals by 2
3  Increment ← WindowSize/4
       // Increment: 75% Overlap, 25% Increment between two adjacent windows
4  NFFT ← Nyquistfrequency
       // NFFT: Number of frequency components
5  for i ← 1 to Channel
6       do FrequencyComponents ← stft(EEGdata(Channel_i), Window,
7                                     WindowSize, Increment, NFFT)
8          AvgFrequencyComponents ← Average(FrequencyComponents)
9          PSD ← 20 x log10(AvgFrequencyComponents/NFFT)
10         PSDBins ← append(PSDBins, Divide(PSD, Bins)
11 return PSDBins
```

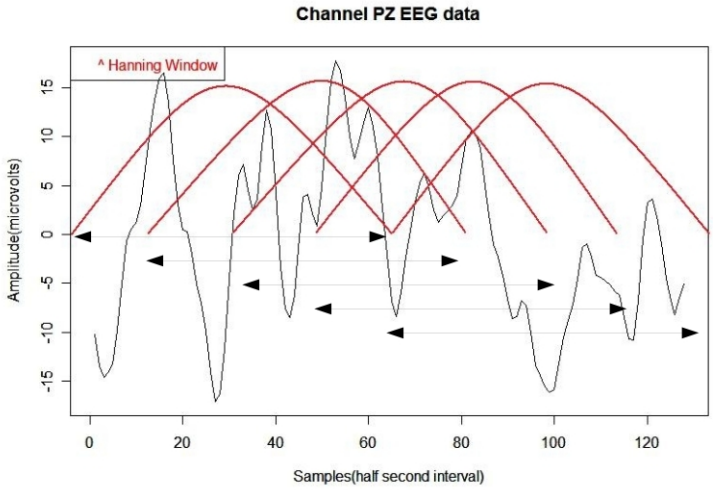

Figure 3.4: Sliding Hanning window over half second of EEG data

Figure 3.4 shows several Hanning windows over half second of EEG data from PZ channel. For this sample window the PSD estimation parameters are No. of samples=128, Window=Hanning, WindowSize=64 samples, Increment=16 samples. The Five Hanning windows correspond to samples 1-64, 16-80, 32-96, 48-112 and 64-128.

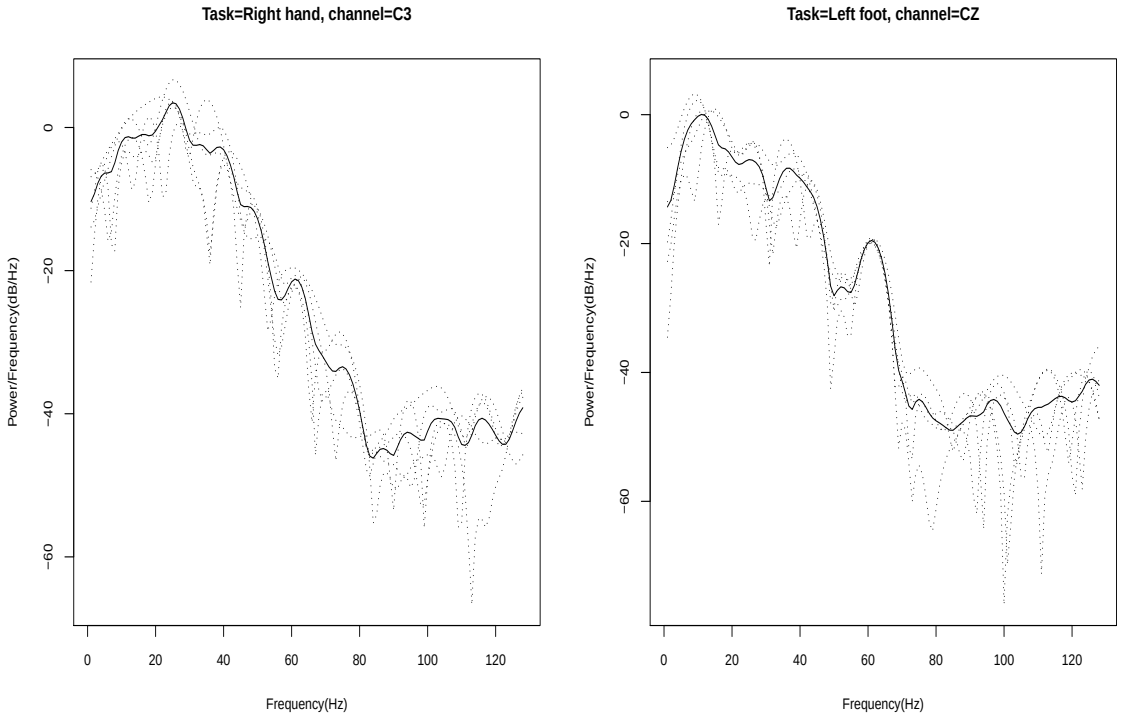

Figure 3.5: Sample PSD estimates for a Right hand (right) and Left foot (left) tasks

The number of frequency components is set to the Nyquist frequency (half the Sampling rate, 128 Hz). The window size, increment percent and the number of frequency components are experiment specific. A wider window accommodates more samples and, therefore results in a finer resolution of the estimated PSD's; on the other hand a wider overlap percentage (smaller increment percentage) causes more windows to slide across and minimizes total variance giving a better estimate of the PSD's. This is an important trade off in the Welch approach. In our experiments we have set the window size to be half the number of samples per second (i.e., we assumed the EEG is stationary over half second intervals) and increment to be 25% of the size of the window. The Short Time Fourier Transform(*stft*) function [28] determines the frequency content of local sections (Hanning window worth of data) of a signal. From a half second of EEG data five PSD's

are estimated corresponding to the five Hanning windows (refer to line 6 in the pseudo code). An average of these five PSD's result in a sample PSD. The sample PSD's are further grouped into frequency bins roughly based on the EEG frequency bands. Sample PSD estimates for an imagined right hand and left foot movements are shown in Figure 3.5. The dotted lines are the PSD estimates from five windows; the solid black line is the average over five windows. It can be seen that for a bodily movement task the power is distributed between 10 Hz to 30 Hz.

3.4 Incremental QDA Algorithm

Quadratic Discriminant Analysis [29] assumes that samples within each class are normally distributed. Figure 3.6 shows sample Quantile-Quantile (QQ) plots on PSD estimates for Fp1 and T4 channels. A 45° line implies that the data is perfectly normal. From offline tests we verified that most channel PSD estimates are near normal. To classify a sample the QDA classifier computes the probability of that sample belonging to each class and makes a decision based on the class with the maximum probability. Using the probability of occurrence of a sample $P(x)$ and the probability of a sample belonging to a class k, $P(C = k)$, we can define $P(C = k, x)$ and $P(x, C = k)$ using the product rule as

$$P(C = k, x) = P(C = k|x)P(x), \tag{3.1}$$

$$P(x, C = k) = P(x|C = k)P(C = k) \tag{3.2}$$

(3.1) and (3.2) represent the same joint probability hence by equating the right sides of (3.1) and (3.2) gives

$$P(C = k|x)P(x) = P(x|C = k)P(C = k) \tag{3.3}$$

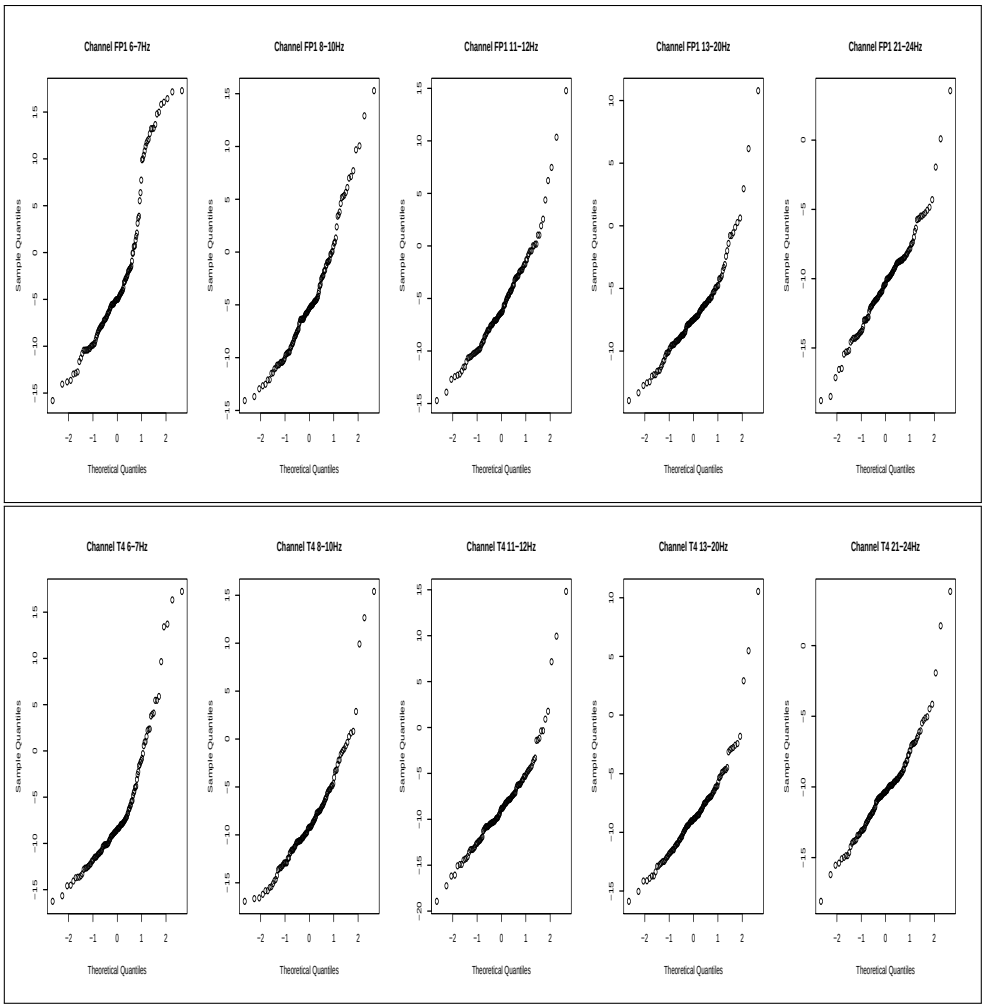

Figure 3.6: Normalcy of PSD estimates. Sample QQ Plots for Fp1 and T4 channel electrode PSD estimates

The above equation can be rearranged to give Baye's rule,

$$P(C = k|x) = \frac{P(x|C = k)P(C = k)}{P(x)} \tag{3.4}$$

From (3.4) The denominator term $P(x)$ is computed by $\sum_{l=1}^{k} P(x|C = l)P(C = l)$ which is the sum of probabilities of a sample belonging to each class over all classes, $P(C = k)$ is the prior probability of a sample from class k; it is 0.5 for two classes with uniform number of samples, 0.25 for four classes with uniform number of samples, etc. $P(x|C = k)$ is the probability of sample x belonging to class k. An important

assumption in QDA is that this probability is modelled by a Gaussian distribution whose probability density function is given by,

$$P(x|C=k) = \frac{1}{2\pi^{\frac{p}{2}}|\Sigma_k|^{\frac{1}{2}}} e^{-\frac{1}{2}(x-\mu_k)^T\Sigma_k^{-1}(x-\mu_k)}, \tag{3.5}$$

where p is the dimension of the data sample, μ_k and Σ_k are the mean and covariance parameters of class k, respectively. To classify a data sample x to belong to class k, we pick the maximum probability $P(x|C=k)$, it is equivalent to picking the $log(P(x|C=k))$,

$$\begin{aligned} \log(P(C=k|x)) &= \log\left(\frac{P(x|C=k)P(C=k)}{P(x)}\right), \\ \log(P(C=k|x)) &= \log(P(x|C=k)) + \log(P(C=k)) \\ &\quad - \log(P(x)) \end{aligned} \tag{3.6}$$

Replacing the $P(x|C=k)$ in (3.6) by its probability density function gives

$$\begin{aligned} \log(P(C=k|x)) &= \log\left(\frac{1}{2\pi^{\frac{p}{2}}|\Sigma_k|^{\frac{1}{2}}} e^{-\frac{1}{2}(x-\mu_k)^T\Sigma_k^{-1}(x-\mu_k)}\right) \\ &\quad + \log(P(C=k)) - \log(P(x)) \end{aligned} \tag{3.7}$$

The right side of (3.7) simplifies to

$$\begin{aligned} \log(P(C=k|x)) &= -\frac{p}{2}\log(2\pi) - \frac{1}{2}\log|\Sigma_k| - \frac{1}{2}(x-\mu_k)^T\Sigma_k^{-1}(x-\mu_k) \\ &\quad + \log(P(C=k)) - \log(P(x)) \end{aligned} \tag{3.8}$$

In a two class problem sample x is said to belong to the class 1 if

$$\log(P(C=1|x)) > \log(P(C=2|x)) \tag{3.9}$$

The general form of (3.9) is given by

$$\arg\max_k \left[\log(P(C=k|x))\right] \tag{3.10}$$

The corresponding general form of a discriminant function for class k is given by

$$\delta_k(x) = -\frac{1}{2}\log|\Sigma_k| - \frac{1}{2}(x-\mu_k)^T\Sigma_k^{-1}(x-\mu_k) + \log(P(C=k)) \tag{3.11}$$

The negative log of the determinant of the covariance matrix can be expressed as the log of the determinant of the inverse covariance matrix [30]. From (3.11) replacing $-\log|\Sigma_k|$ by $\log|\Sigma_k^{-1}|$ gives

$$\delta_k(x) = \frac{1}{2}\log|\Sigma_k^{-1}| - \frac{1}{2}(x-\mu_k)^T\Sigma_k^{-1}(x-\mu_k) + \log(P(C=k)) \tag{3.12}$$

Hence the mean and inverse covariance matrix are the only parameters that are needed to determine the probability of a sample belonging to class k. In an incremental QDA algorithm we are dealing with data samples as they arrive. Hence when the x_l^{th} sample arrives, assuming $\mu_{k,(1:l-1)}$ represents the mean up until x_{l-1}^{th} sample, the mean can be updated as,

$$\mu_{k,(1:l)} = \frac{(\mu_{k,(1:l-1)}(l-1)) + x_l}{l} \tag{3.13}$$

The inverse covariance matrix can also be updated an incremental fashion. This is our modification of Berge, et al., nonincremental method [30]. We represent the inverse covariance matrix by Cholesky Decomposition as

$$\Sigma_k^{-1} = L_k^T D_k L_k, \tag{3.14}$$

where L_k is a lower triangle matrix and D_k is a diagonal matrix for class k. To estimate the inverse covariance matrix we will need to estimate the L and D matrices for k^{th}

class using N_k training samples. From (3.12) replacing the inverse covariance matrix with the modified Cholesky decomposition results in

$$\begin{aligned}\sum_{i=1}^{N_k}\log(P(C=k|x)) &= \sum_{i=1}^{N_k}\left[\frac{1}{2}\log|L_k^T D_k L_k| - \frac{1}{2}(x_i-\mu_k)^T L_k^T D_k L_k (x_i-\mu_k)\right] \\ &\quad + \sum_{i=1}^{N_k}\left[\log(P(C=k))\right], \end{aligned} \tag{3.15}$$

where N_k is the number of samples in class k and x_i is the i^{th} sample in the k^{th} class. Further L_k can be expressed as $I - B_k$, where B_k is the lower triangular matrix with zeros on the principle diagonal and I is the identity matrix. This gives

$$\begin{aligned}\sum_{i=1}^{N_k}\log(P(C=k|x)) &= \sum_{i=1}^{N_k}\left[\frac{1}{2}\log|(I-B_k)^T D_k (I-B_k)|\right] \\ &\quad - \sum_{i=1}^{N_k}\left[\frac{1}{2}(x_i-\mu_k)^T (I-B_k)^T D_k (I-B_k)(x_i-\mu_k)\right] \\ &\quad + \sum_{i=1}^{N_k}\left[\log(P(C=k))\right] \end{aligned} \tag{3.16}$$

The determinant of $I - B_k$ is 1 by definition hence the first term in (3.16) simplifies to $\log|D_k|$. Representing the mean subtracted i^{th} sample in the k^{th} class i.e., $(x_i - \mu_k)$ by $V_{k,i}$; the log-likelihood of (3.16) with respect to (B_k, D_k) becomes proportional [30] to

$$\begin{aligned}\sum_{i=1}^{N_k}\log(P(C=k|x)) &= \sum_{i=1}^{N_k}\left[\frac{1}{2}\log|D_k| - \frac{1}{2}(((I-B_k)^T V_{k,i})^T D_k (I-B_k)^T V_{k,i})\right] \\ &\quad + \sum_{i=1}^{N_k}\left[\log(P(C=k))\right] \end{aligned} \tag{3.17}$$

Rearranging (3.17) results in

$$\sum_{i=1}^{N_k}\log(P(C=k|x)) = \sum_{i=1}^{N_k}\left[\frac{1}{2}\sum_{r=1}^{p}\log d_{k,r}\right]$$

$$-\sum_{i=1}^{N_k}\left[\frac{1}{2}\sum_{r=1}^{p}\left(V_{k,i,r}-B_{k,r,1:(r-1)}^{T}V_{k,i,1:(r-1)}\right)^2 d_{k,r}\right]$$
$$-\sum_{i=1}^{N_k}\left[\frac{1}{2}\log(P(C=k))\right], \tag{3.18}$$

where

- p is the number of features of a data sample also it is the number of rows/columns in the inverse covariance matrix,
- $d_{k,r}$ is the r^{th} diagonal entry (same row-column intercept) in the D_k matrix,
- $V_{k,i,1:(r-1)}$ is r^{th} row comprising of 1 to r-1 column entries in the k^{th} class (V is the mean subtracted sample ($x_i - \mu_k$)), and
- $B_{k,r,1:(r-1)}$ is r^{th} row comprising of 1 to r-1 column entries in the k^{th} class (Lower triangular matrix excluding the diagonal entries).

Differentiating (3.18) with respect to $B_{k,r,1:(r-1)}$ and $d_{k,r}$ to maximize the likelihood of $B_{k,r,1:(r-1)}$ and $d_{k,r}$ and equating it to zero along with some rearranging results in estimates of B_k and $d_{k,r}$

$$B_{k,r,1:(r-1)} = \frac{V_{k,i,r}V_{k,i,1:(r-1)}^{T}}{V_{k,i,1:(r-1)}V_{k,i,1:(r-1)}^{T}}, \tag{3.19}$$

$$d_{k,r} = \frac{N_k - 1}{[V_{k,i,r} - B_{k,r,1:(r-1)}^{T}V_{k,i,1:(r-1)}]^2} \tag{3.20}$$

For N_k samples from k^{th} class, the corresponding B and d matrices can be updated as,

$$B_{k,r,1:(r-1)} = \frac{\sum_{i=1}^{N_k} V_{k,i,r}V_{k,i,1:(r-1)}^{T}}{\sum_{i=1}^{N_k} V_{k,i,1:(r-1)}V_{k,i,1:(r-1)}^{T}}, \tag{3.21}$$

$$d_{k,r} = \frac{N_k - 1}{\sum_{i=1}^{N_k}[V_{k,i,r} - B_{k,r,1:(r-1)}^{T}V_{k,i,1:(r-1)}]^2} \tag{3.22}$$

Using (3.21) and (3.22) the complete lower triangular matrix is estimated as,

ESTIMATEINVERSECOVMATRIX($sample_{ki}$)

1 **for** $m \leftarrow 1$ **to** $rows$ // $rows$ is the number of rows in the inverse covariance matrix
2 **do for** $n \leftarrow 1$ **to** $m - 1$
3 **do** $Update\ B_{k,m,n}$
4 $Update\ D_{k,m,m}$
5 **return** B_k, D_k

	1	2	3	4	5
1	A				
2	1	B			
3	2	3	C		
4	4	5	6	D	
5	7	8	9	10	E

Figure 3.7: The Inverse Covariance matrix for a small 5 feature dataset

Line 3 in the *EstimateInverseCovMatrix* pseudo code, corresponding to (3.21), can be viewed as updating the lower triangular matrix (entries 1 through 10) in Figure 3.7 and line 4 can be viewed as updating the diagonal entries (letters A through E), corresponding to (3.22). Notice that the B matrix will need to be updated before being used in the D matrix computation. In case all samples were accumulated and the inverse covariance matrix is estimated, then the estimated inverse covariance matrix would be same as the computed inverse covariance matrix, subject to the N or $N - 1$ scaling.

3.5 Divergence between Computed and Estimated parameter distributions

We attempted to quantify how far the estimated parameters are from the computed parameters. We treated the computed parameters as modeling one distribution and the in-

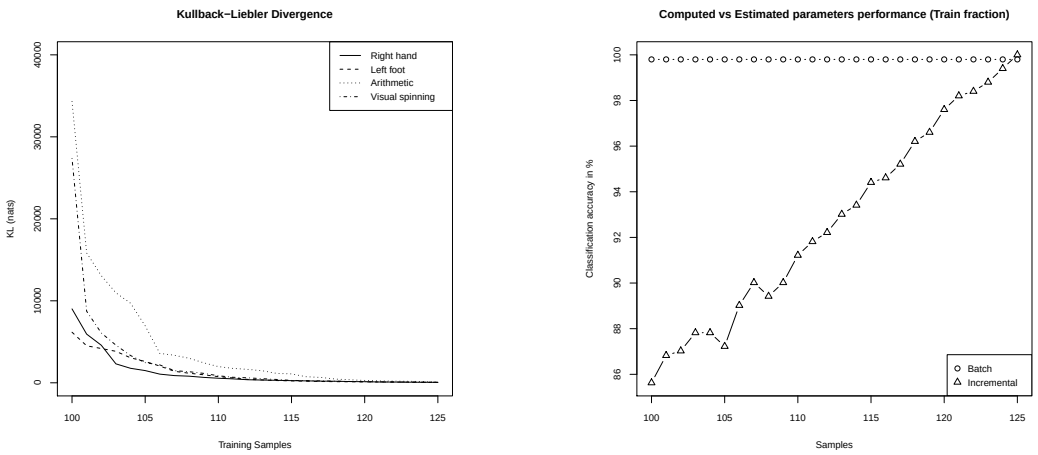

(a) (b)

Figure 3.8: Kullback-Leibler divergence for all four tasks (left) and the associated performance on a four task problem (right)

crementally estimated parameters modeling another. The Kullback-Leibler divergence gives the relative entropy or divergence between an unknown distribution $p(x)$ and an approximating or model distribution $q(x)$ [29]. It is an asymmetrical quantity. The divergence is in nat units. The general form of Kullback-Leibler divergence [29] is,

$$D_{KL}(p||q) = -\int p(x) \ln \left(\frac{q(x)}{p(x)} \right) dx$$

For two multivariate distributions $N_c(\mu_c, \Sigma_c^{-1})$ and $N_e(\mu_e, \Sigma_e^{-1})$ the closed form of Kullback-Leibler divergence [31] is given by,

$$\begin{aligned} D_{KL}(N(\mu_c, \Sigma_c^{-1})||N(\mu_e, \Sigma_e^{-1})) &= \frac{1}{2}\left(\log\left(\frac{|\Sigma_c^{-1}|}{|\Sigma_e^{-1}|} \right) + trace(\Sigma_e^{-1}\Sigma_c) \right) \\ &\quad + \frac{1}{2}\left((\mu_c - \mu_e)^T \Sigma_e^{-1} (\mu_c - \mu_e) - N \right), \end{aligned} \quad (3.23)$$

where μ_c and Σ_c^{-1} are the computed mean and inverse covariance parameters, μ_e and Σ_e^{-1} are the incrementally estimated mean and inverse covariance parameters, N is the number of features/attributes in the distributions. Equation (3.23) uses the inverse covariance parameter consistent with the parameters estimated in this project; to use the

covariance parameter (3.23) will need to be modified accordingly. We used the *kl.div()* [32] function in R to compute the KL divergence as samples are added incrementally. Figure 3.8(a) shows the KL divergence for the computed and estimated parameter distributions for all four tasks from the sample dataset. Along the x-axis are the training samples (from train sequences 1-13 only $\sim$ 125 samples per task) starting from 100 samples. On the y-axis is the KL divergence in nats. We can observe that the divergence drops steadily as training samples are added one at a time. The final divergence, when all samples are added, for the four tasks vary between 50 and 70 nats. Using all twenty sequences from the dataset ($\sim$ 190 samples per task) resulted in final divergences varying between 15 and 25 nats. We hypothesize as more training samples are added this divergence will approach zero. The associated performance of the incremental classifier on the training fraction (trained and tested on the same fraction) on a four task problem is shown in Figure 3.8(b). We see that as samples are added the incremental QDA performance gradually approaches batch QDA performance.

3.6 Feature Selection

Feature selection is primarily performed to select relevant and informative features [33]. Feature selection approaches are roughly categorized into Predictor, Filter and Wrapper methods [33]. Filters rank features based on the training samples filtering out features that are irrelevant. In the BCI applications we perform feature selection to improve performance, use the selected features to understand the underlying brain activity and lastly reduce the number of features thereby the number of parameters to be estimated. In EEG frequency domain the features are the power spectral densities organized into frequency bins in each channel. For instance organizing the PSD's into five bins results in 95 (19 channels $\times$ 5 bins each) features.

3.6.1 The Relief Algorithm

The Relief [34] algorithm is a filter based feature selector. It is time-efficient and computationally less expensive. It takes one parameter, the number of iterations, to rank features. This parameter is experiment specific as it depends on the number of samples, quality of EEG data, sampling rate and tasks (overlapping/non-overlapping) to be classified.

The Relief algorithm works by randomly selecting a sample from the training set, finding a nearest hit (sample closest in Euclidean distance from the same class) and nearest miss (sample closest in Euclidean distance from a different class) [34]. Individual weights are associated with each feature. Using the nearest hit and nearest miss the weights are updated by a fraction of a diff factor. This diff factor is computed as,

$$diff(feature, S_1, S_2) = \frac{|value(feature, S_1) - value(feature, S_2)|}{max(feature) - min(feature)},$$

where S_1 is the randomly chosen sample and S_2 is the nearest hit/miss, respectively. The intuition behind Relief is that the features that help recognize the nearest hit are not so interesting hence decrease their weights and the features that help recognize the nearest miss are the desirable ones hence increase their weights. This process is repeated for a set number of iterations which is also the only parameter to this algorithm. After completion of all iterations sort the updated weights and choose all features with positive weights. The pseudo code for Relief algorithm is below,

RELIEF($features, iterations, Train_{data}$)

```
1  W[1 : features] ← 0        // Weight vector of length features
2  for i ← 1 to iterations
3       do Randomly select a sample R_i from Train_data
4          H_i ← nearesthit(R_i, Train_data)
                              // H_i: Same class as the random sample R_i
5          M_i ← nearestmiss(R_i, Train_data)
                              // M_i: Different class from the random sample R_i
6          for k ← 1 to features
7               do W[k] ← W[k] − diff(k, R_i, H_i)/iterations+
8                                diff(k, R_i, M_i)/iterations
9  return W
```

Note: The Relief algorithm presented above is for a two class problem. Relief can be extended to multiple classes [34].

3.6.2 Preprocessing

Prior to feature selection the associated preprocessing will need to performed. We begin with the QDA discriminant function

$$\delta_k(x) = \frac{1}{2}\log|\Sigma_k^{-1}| - \frac{1}{2}(x-\mu_k)^T\Sigma_k^{-1}(x-\mu_k) + \log P(C=k)$$

Ideally we would like the feature selector to rank the features in the inverse covariance matrix that in a way correspond to the product $(x-\mu_k)^T\ (x-\mu_k)$ from the equation above. Hence we perform some preprocessing to ready the data for feature selection. Each entry in the inverse covariance matrix corresponds to the interaction between, for instance, feature a and feature b. We would like Relief to rank this interaction between pairs of features over individual features. So taking into consideration the interaction between all possible pairs of N individual features results in N^2 features. From this N^2 features only $N \times (N+1)/2$ features are unique since the upper triangular matrix is a mirror image of the lower triangular matrix. The preprocessing will first require each feature to be mean subtracted before taking the product. Refer to the *Compute* pseudo code below,

COMPUTE($features, PSDSamples$)

```
1   for i ← 1 to features
        //features is the number of rows/columns in the inverse covariance matrix
2       do feature_1 ← PSDSamples(i^th feature)
3          mean_1 ← mean(feature_1)
4          for j ← i to features
5              do feature_2 ← PSDSamples(j^th feature)
6                 mean_2 ← mean(feature_2)
7                 data_return ← append[data_return, ((feature_1 − mean_1)
8                                                    x (feature_2 − mean_2))]
9                 features_updated ← features_updated + 1
10  return data_return, features_updated
```

This process is repeated for all entries in the lower triangular matrix (upper triangular matrix is a mirror image of the lower triangular matrix) of the inverse covariance matrix. The diagonal entries are mean subtracted and squared. The $features_{updated}$ and $data_{return}$ (line 9) are fed as $features$ and $Train_{data}$, respectively, to the *Relief()* function above. This will drastically blow up the number of features but it gives better control over feature selection. For instance EEG samples from 19 channels organized into 5 frequency bins results in a total of 95 features. Further these 95 features are mean subtracted and multiplied to get (95 $\times$ 94 / 2) 4465 features which Relief ranks. The top ranking features are added in a forward selection manner (which implies the lower and upper triangular matrix entries are set to their respective estimates while low ranking feature entries are set to zero). By default all diagonal entries are set to their estimates irrespective of their ranks as this will ensure that the determinant of the inverse covariance matrix exists. The number of Relief iterations is bounded by the number of samples in the training partition. We have tested the number of iterations to vary between 50% to 90% of the total number of samples (in training partition). By estimating the PSD's the total number of samples shrink (128 raw EEG samples translate into one PSD sample) hence it does not make a significant difference in terms of execution time when the iterations vary between 50% to 90%. The complexity of the task and the ease with which

a subject can perform the task will dictate how many iterations Relief will need to pick the most significant features. In our experiments we have fixed the number of iterations to 90% of the total number of samples which roughly translates to 226 iterations.

Chapter 4

Results

This chapter presents the results from two experiments. From the previous chapter Section 3.3 gives the technical details of the data set used in both experiments. Sections 3.4 and 3.7 gives the parameter settings for the power spectral density estimation and the Relief feature selection.

4.1 Experiment I

In experiment I we evaluate the performance of the proposed BCI model on a two task problem. The two chosen tasks are imagination of right hand movement and visual spinning of a three dimensional object.

In the first task the subject was trying to imagine holding a ball, thrown at him, with his right hand palm facing upwards. This is a motor imagery task that can be performed in two ways; one, kinesthetic imagery (KI) where the subject imagines performing the task; two, visual imagery (VI) in which the subject visualizes performing the task. Doyon, et al., reports that KI and VI mediate separate neural systems, which contribute differently during processes of motor learning and neurological rehabilitation [35]. Numerous studies have also shown that areas of the brain overlap in motor imagery (KI) and motor executing tasks (actual movement) and that these areas are not generally active during visual imagery [36]. Regarding regions of the brain that are active in

motor imagery tasks, altered activation has been reported in parietal and premotor areas during movement imagination [37]. Both areas have also been associated with mental representation of movement [38]. Pfurtscheller, et al., suggests that motor imagery activates primary sensorimotor cortex (S1 area) [39]. There is conflicting evidence regarding the involvement of primary motor cortex (M1 area) [40]. As far as frequencies are concerned, actual movement tasks are associated with suppression of alpha waves and exhibition of strong beta waves [41].

In the second task the subject was visualizing a laptop computer spinning around. The mental rotation is a visual imagery task. There is a lot of overlap in functions and representations between visual imagery and visual perception [42, 43]. Among others the visual rotation task is affected by

- the view of the object: canonical or non canonical views cause different regions of activation in the brain [43];
- dimensionality of the object: two dimensional object rotation has higher EEG frequency power when compared to three dimensional object rotation [44];
- subject gender accounts for changes during the mental rotation task [27];
- visual imagery arises from interaction between a host of sub processes [36].

The frequencies of the visual spinning task are spread over theta, alpha and beta frequency ranges [27]. Whether imagination of these tasks will trigger activity in the same frequencies is questionable.

These two tasks were chosen from the original four task experiment since they involve two distinct regions of activation in the brain. In theory the right hand movement task activates regions of the brain in the left central and left frontal lobes (contralateral to the hand). The visual spinning task activates the primary visual cortex in the occipital

lobe. Whether imagination of these tasks activates similar regions of the brain is subject to argument. Berthoz, et al., gives counter evidence that transformation of mental images are in part guided by motor processes even in the case of objects rather than body parts [45]. In view of this evidence the theory that these two tasks activating different regions of the brain does not hold. Nevertheless good recognition rates by the BCI on a two task problem would lead us to some insight into the number of features selected, what channel-frequency components are highly ranked and the interaction between these features.

In the BCI offline mode we performed the following steps. First, the dataset is partitioned into train, validation and test.Then, the BCI is trained on the train partition and also rank the features are ranked on the same. Next the features are added in a forward selection manner on the validation partition to identify the peak performance and the associated set of top features that caused the peak performance. Finally the set of top ranked features are used on the test partition to evaluate the performance.

Figure 4.1 is a performance plot of the BCI model when averaged over multiple runs since our feature selection (i.e., Relief) approach incorporates an element of randomness in the way of selection of samples. Also the results were stable and the trends captured better when averaged over multiple runs. From pilot experiments the trends observed were stable over ten iterations or so. Along the x-axis are the features added ten at a time in a forward selection manner as ranked by Relief on the train partition. We use the classification accuracy as a performance metric i.e., given a PSD sample the task it is associated with to by the BCI model is checked against its original target task. The number of correctly recognized samples are plotted as a percentage of the total number of samples along the y-axis. The following paragraphs explain each part of the figure,

The points: All plots are averaged over ten iterations. The gray, thick black and solid black lines correspond to the performances of incremental QDA (using estimated pa-

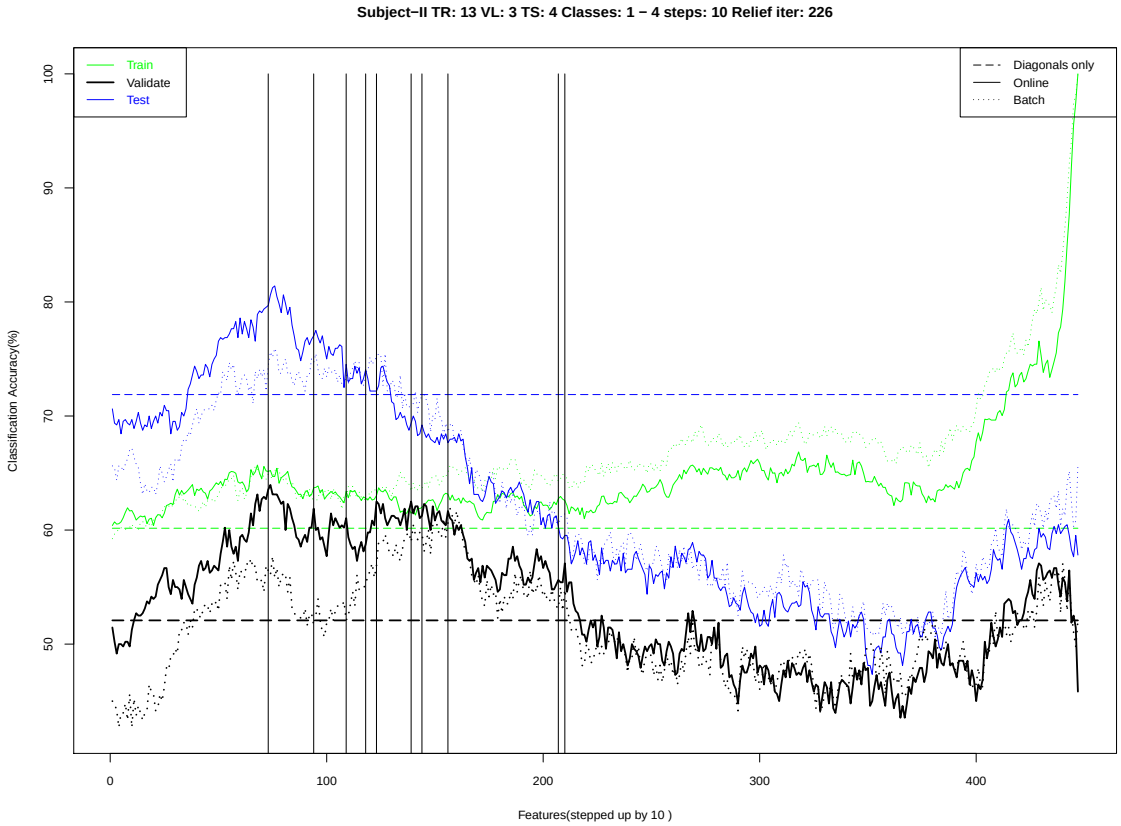

Figure 4.1: Experiment I performance plot

rameters) on train, validation and test partitions, respectively. The closely associated dotted lines correspond to the batch QDA performances (parameters are computed) on the same three partitions. From the twenty sequences that make up the data set, 13 sequences (65%) went into training and ranking the features, 3 sequences (15%) went into validating the ranked features and 4 sequences (20%) went into testing the performance. All sequences are ordered by time in the sense the train sequences were recorded first, followed by the validation and finally the test set. Since the partitions, hence the PSD samples, are the same for incremental and batch mode performing feature selection in each mode is the same as performing Relief twice in any one mode. Since our results are an average over ten iterations we performed feature selection only once in the incre-

mental mode. The top ranking features from the incremental mode are also added in a forward selection manner in the batch mode. The plots reveal that batch and incremental QDA performances are consistent. Observe that the incremental QDA plots tend to converge with the batch QDA plots for all three partitions when all features are added (extreme right) to the inverse covariance matrix.

The horizontal lines: The three dashed lines from top down correspond to BCI performance with only the diagonal entries for the test, train and validation partitions, respectively. Recall that our feature selector ranks the features in the lower triangular matrix of the inverse covariance matrix. In the forward selection approach we start with a diagonal inverse covariance matrix and subsequently add ten features at a time. Hence the dashed line corresponds to the diagonal inverse covariance matrix with no features added. Essentially it is the inverse covariance matrix with variances only.

The vertical lines: The vertical lines correspond to the peaks in the validation set in the ten iterations. Although we would like to mention that a different partition of the train, validation and test would generate different plots.

From Figure 4.1 it can be observed that the validation and test partitions follow similar trends. On the other hand the train partition follows a different trend following the addition of 200 features. This trend will need to be further investigated; we speculate that it is data dependent as with other datasets different trends were observable. Starting with the diagonal inverse covariance matrix the test performance (solid black line) vibrates around the first thirty features, rises steadily from 30-80 features and peaks around 80-90 features then it begins to decline sharply until 250 features. Between 250 to 280 features the performances show a small bump following which they reach the lowest point. When all features are added to the inverse covariance matrix the inverse covariance matrices in the batch and incremental approach are essentially the same, subject to computation or estimation, but the performances still vary because the latter

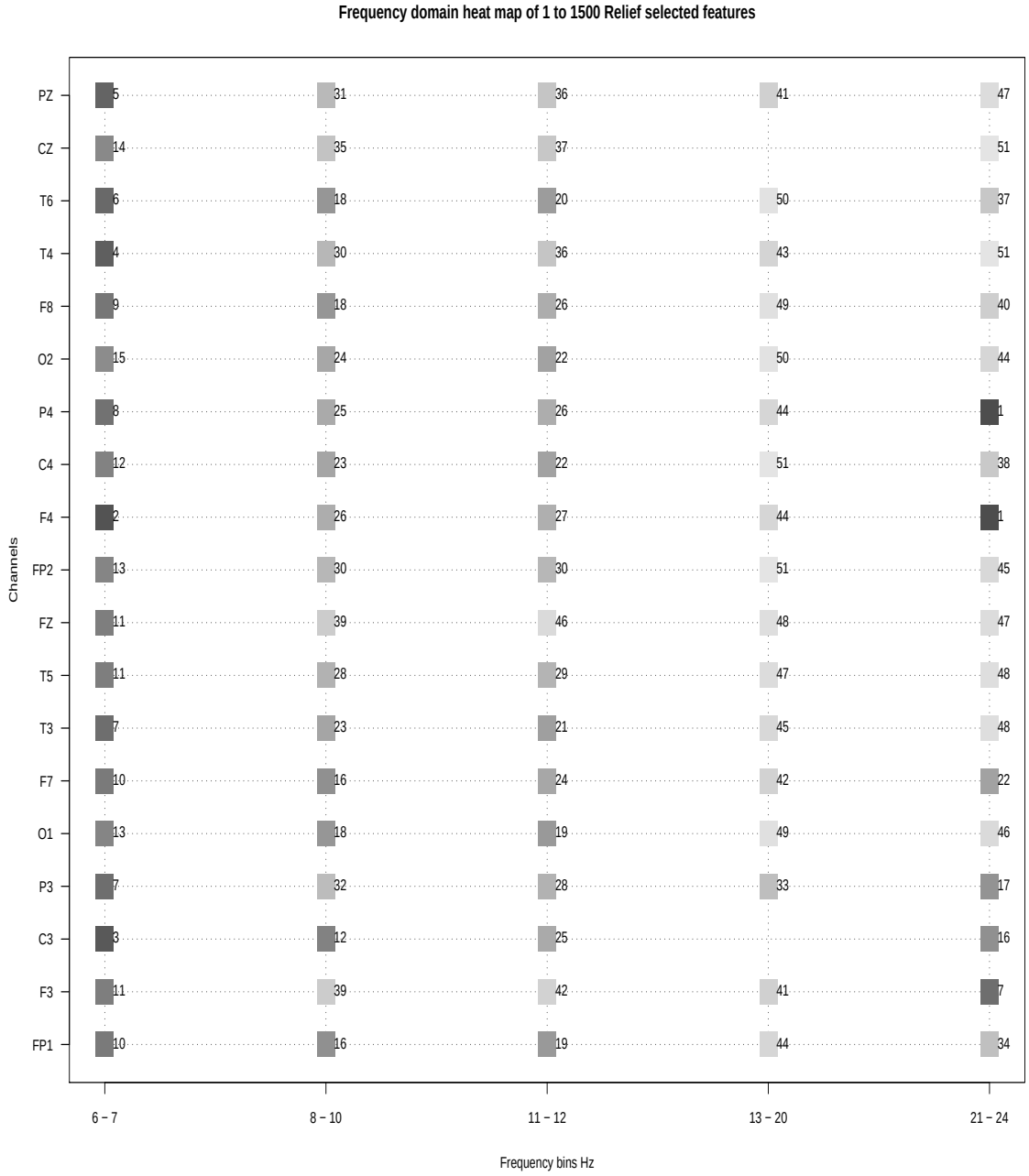

Figure 4.2: Experiment I 1 to 1500 features heat map

is estimated and the former is computed. Table 4.1 shows the mean performance of the proposed BCI for experiment I over ten iterations on the test partition. The three

Table 4.1: Comparison of performances on test partition for experiment I

	Diagonals only	**With Feature Selection**	**Without Feature Selection**
Batch QDA	67.20%	69.53%	65.01%
Incremental QDA	71.88%	73.75%	57.81%

columns correspond to the sparsity of the inverse covariance matrix. The first column corresponds to the performance only when the diagonal entries are added in the inverse covariance matrix. The second column corresponds to peak performance when adding ten features at a time in a forward selection manner and the last column corresponds to a completely filled inverse covariance matrix. The test partition's mean performance and standard deviation with feature selection is $73.75\% \pm 7.39\%$. Excluding the two outlier performances gives a 77%. Note that even though the average performance peak from the plot is around $84.53\% \pm 1.15\%$ all ten iterations (vertical lines) do not coincide with the peak hence the difference.

Along with the performance we are also interested in the top features ranked by Relief and added in the forward selection manner which caused the performances to spike around 80-90 features on an average. Figure 4.2 is a heat map of the top 150 features ranked in the train partition. A dark shaded box corresponds to a higher rank. Note that we are adding ten features at a time hence 150 features translates to 1500 (150 x 10) features. Along the x-axis are the frequency bins and along y-axis are the channel electrodes. Recall when a feature is added essentially we are setting its inverse covariance matrix entry to be non zero. An inverse covariance matrix entry is the interaction between channel a at bin b with channel c at bin d. For example Fp1 6-7 Hz interacts with F4 21-24 Hz. This causes the corresponding Fp1 6-7 Hz and F4 21-24 Hz heat map entry to be incremented by one. In this manner the top 1500 features are tracked

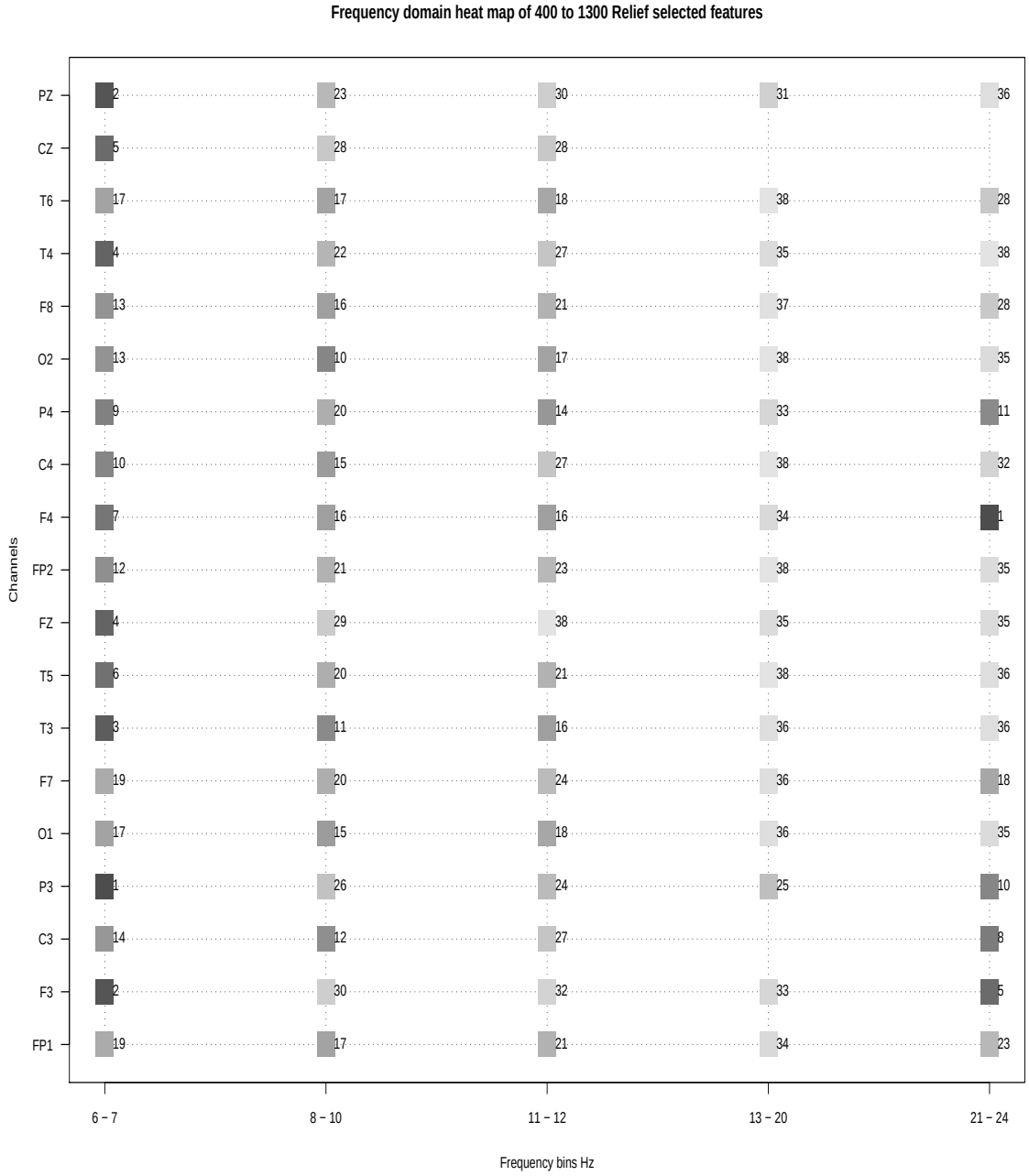

Figure 4.3: Experiment I 400 to 1300 features heat map

over all ten iterations and an average is plotted in Figure 4.2. To get a sense for the contributing features, P4 21-24 Hz which ranks 1 translates to 2.69% (approximately

in 807 instances P4 21-24 Hz is paired with another feature) and T4 21-24 Hz which ranks 51 translates to 0.06% of the total occurrences over ten iterations. Our hypothesis on selection of channel electrodes given the tasks are the electrodes spread over the left central, left frontal and occipital lobes. Relief ranked in order the channels P4, F4, C3, T4, PZ, T6, F3, F8, Fp1, etc. Other than C3 and F3 there is some inconsistency on the ranked channels as they are spread over the parietal, right frontal and right temporal lobes. One simple explanation is the convoluted nature of the brain and neuron firing properties that electrodes around the central (P4, F4, T4, PZ, F3) and occipital (P4, PZ, T6) lobes are picking up more signals then the ones actually above them. In total 14 features (including ties) rank among the top ten of which eleven lie in the theta (6-7 Hz) range and three lie in the beta 2 (21-24 Hz) range. Within the top 20 only eight features lie between 8-20 Hz. This led us to believe that the heat map which represents the top 1500 features include features that cause the dip in the performance and is not very specific. Hence we narrowed down our heat map representation to the features that actually caused the spike in the validation and test partitions.

The top 900 features ranked between 400^{th} to 1300^{th} added features, centered around the spike, were further analyzed in Figure 4.3. From this heat map among the top ranked channels in order are F4, P3, F3, PZ, T3, T4, FZ, CZ, T5, C3, P4, C4, etc among which F4, F3 and P3 are contributing two bins each. It can also be seen that this heat map projects a different set of channels as top ranked when compared to the previous heat map. Eleven of the top ten features (including ties) lie in the 6-7 Hz theta bin and four of the top ten features lie in the beta 2 range. Also there is a lot of activity in the 8-20 Hz band, eighteen of the top 20 features lie in this range when compared to eight in the previous heat map. This suggests that more alpha and beta 1 features causes an increase in performance. In all of the ten iterations we find the right hand task dominating the visual imagery task in terms of recognition rates. This may be because

the features selected aid in recognizing the right hand task over the visual spinning task. Examining these channels more closely we find channels are being represented from the contralateral side, ipsilateral side and along the line which divides the two hemispheres. We, along with Lee, et al., [46] claim that it is difficult to find significant contralateral characteristics in motor imagery tasks.

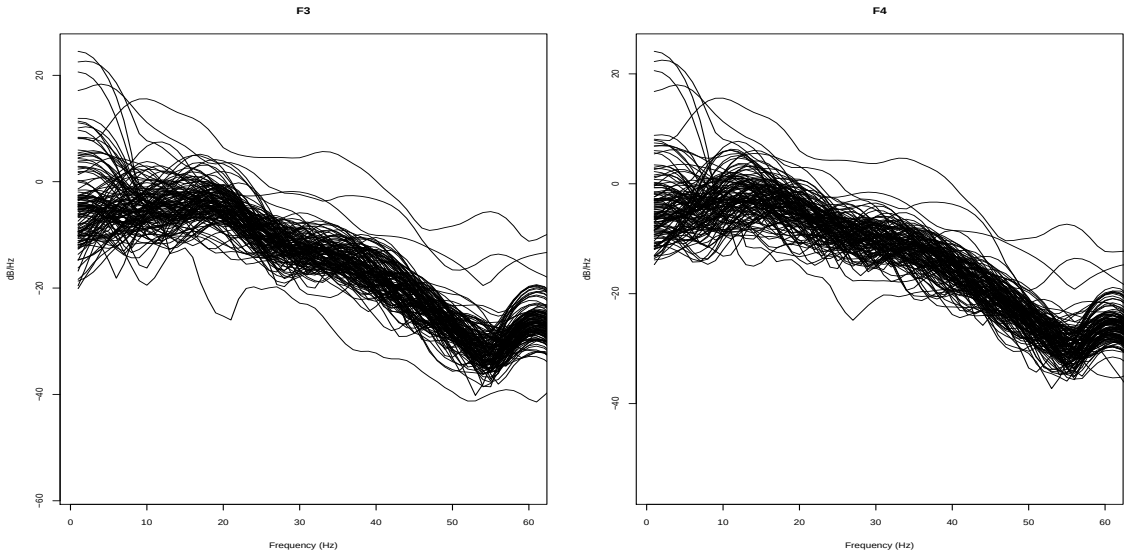

Figure 4.4: Experiment I PSD's of F3 and F4 electrodes for the right hand task on the train partition

We speculate that more ipsilateral channel electrodes are chosen as event-related synchronization (ERS) is present in the ipsilateral side when imagining a right hand task. Increase in rhythmic activity or synchrony (reflected in the appearance of a spectral peak) due to internally or externally paced events is event-related synchronization (ERS) and the decrease is event-related desynchronization (ERD) [47, 48]. ERD has been reported to be a characteristics of voluntary muscle movement [49]. Several studies claim that in motor imagery tasks there is dominating EEG activity in the ipsilateral side then the contralateral sighting ERS and ERD phenomenon [49, 50]. Pfurtscheller, et al., reports something very similar that in a motor imagery task a contralateral ERD

dominates an ipsilateral ERS on no feedback sessions, at the onset of the visual cue, following feedback the ipsilateral ERS becomes apparent [48]. Beisteiner, et al., also reports widespread DC potential over the contralateral and ipsilateral sides for motor imagery tasks [51]. Spatial patterns on imagery tasks exhibit relative increase in EEG variance focused on the ipsilateral side and ERD in the contralateral primary sensorimotor area [52]. Kamousi, et al., adopts an inverse problem approach to classify motor imagery tasks using source reconstruction. They claim that during motor imagery a decrease in synchrony of the underlying neuronal population causes a decrease of power in the alpha rhythm in the contralateral side and subsequently stronger activity is reported on the ipsilateral side [53].

Again these results are based on studies that used single trial EEG in which ERD and ERS components can be clearly identified. In our experiment the subject repeatedly performed all tasks following visual cues at one sitting. Based on these findings we speculate that a right hand imagery task could cause the contralateral channels to have smaller spectral peaks, resulting in low power when compared to the channels in the ipsilateral side. The variance in EEG activity in those channels causes Relief to pick those channels over the others. Figure 4.4 shows the estimated PSD's for right hand task on the F3 (contralateral) and F4 (ipsilateral) channels from the training partition which are both ranked highly by Relief. It can be observed that F3's peak is shifted yet tightly coupled around 20 Hz when compared to F4 which shows a lot of variance in activity around 10 Hz. In addition to channels on the ipsilateral side being chosen more often we also probed into why the theta bins are chosen more often than the other bins. Theta oscillations are related to episodic memory process responsible for orientation in space and time [54]. Increase in theta activity is reported during retention and working memory tasks and motor imagery is associated with working memory [55, 56]. From Figure 4.4 notice there is also a lot of variance in the lower frequencies (1-10 Hz). We

believe this is due to the half second sliding Hanning window placed over a complete sequence of EEG data. So there could be instances in which the window is breaking up a right hand task over two subsequent PSD estimates or maybe even one windows worth of samples (128 samples) is not enough to capture a snapshot of a complete right hand task which the subject performs repeatedly.

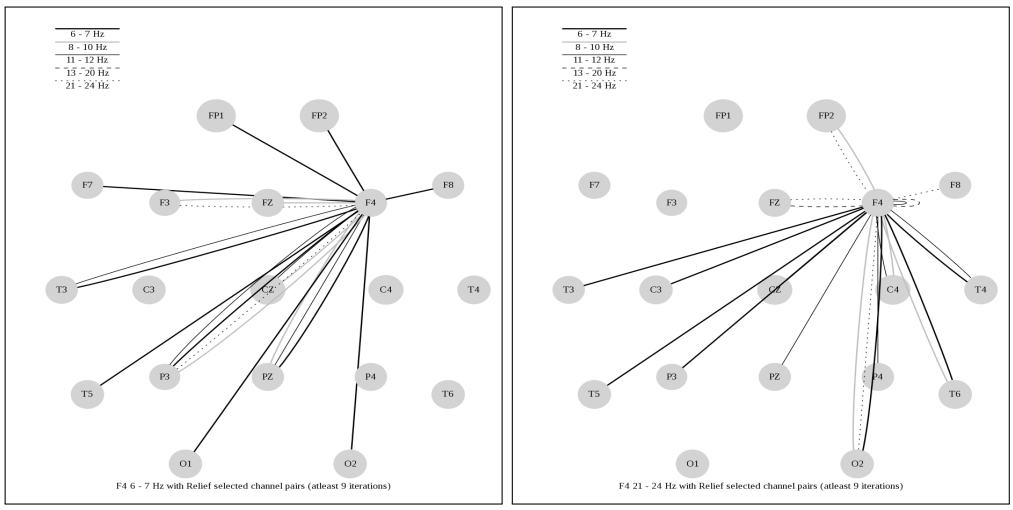

Figure 4.5: Experiment I F4 at 6-7 Hz (left) and F4 at 21-24 Hz (right)

From the heat map presented above we are interested in which channels the top channels are frequently paired with. Among the top ten features F4, F3 and P3 have two bins each in the 6-7 Hz and 21-24 Hz, respectively. Figure 4.5 is a snapshot of the F4 electrode at the two frequency bins: 6-7 Hz (left) and 21-24 Hz (right). Each interaction is represented by a line. The target electrode frequency bin determines the line style, viz. 6-7 Hz by bold(black), 8-10 Hz by bold (gray), 11-12 Hz by solid, 13-20 Hz by dashed and 21-24 Hz by dotted. There are instances where more than one line exists between channels; this implies that the source electrode interacts with more than one bin at the target electrode. A pair of lines exist only if they occur in nine or more of the ten runs per experiment. F4 at 6-7 Hz (left) is more sparsely connected then F4 at 21-24 Hz (right), consistent with the ranks. F4 at 6-7 Hz is highly concentrated within the F3-O1

arc. F4 21-24 Hz is highly dominated by the 6-7 Hz bins along the temporal, occipital and parietal lobes. Figure 4.6 shows the same graph for F3 channel at two bins 6-7 Hz (left) and 21-24 Hz (right). Here the sparsely linked F3 at 6-7 Hz is highly ranked when compared to the 21-24 Hz bin. F3 also tends it pair with itself at other frequency bins. Figure 4.7 shows P3 channel pairs. P3 does not seem to interact with channels at 13-20 Hz. P3 at 21-24 Hz is in a closed loop between T5 and P4. From these plots there seems to be no visible relationship between the given tasks and the interacting channel pairs.

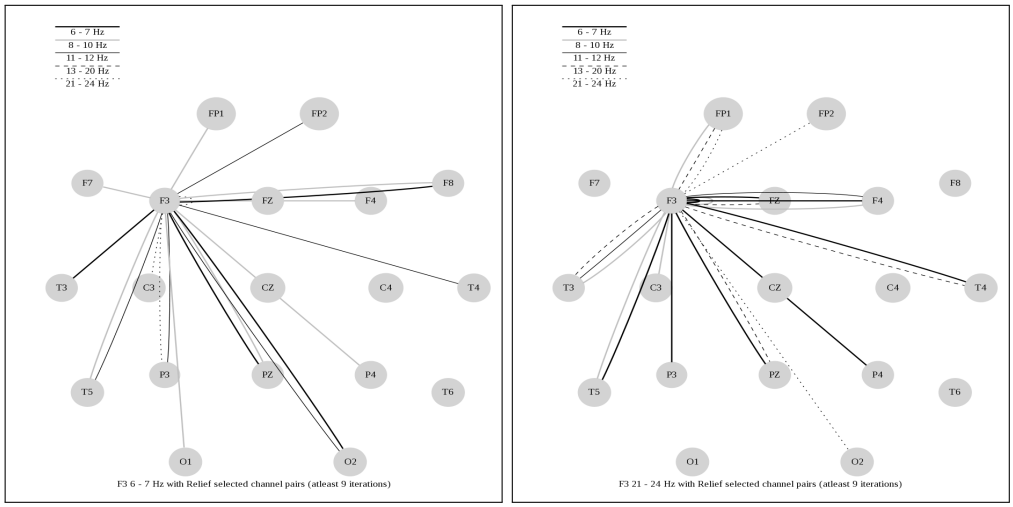

Figure 4.6: Experiment I F3 at 6-7 Hz (left) and F3 at 21-24 Hz (right)

4.2 Experiment II

In experiment II we evaluate the performance of the proposed BCI model on another set of two tasks. The first task is same as the first task in experiment I. In the second task the subject imagines tapping the left foot repeatedly. Both are motor imagery tasks and triggers activation in the parietal and premotor areas [37, 38].

The details of the plot in Figure 4.8 are identical to experiment I. The frequency components that seemed to work for experiment I do not work so well for experiment II. Additionally the performances were unstable over ten iterations hence we plotted them

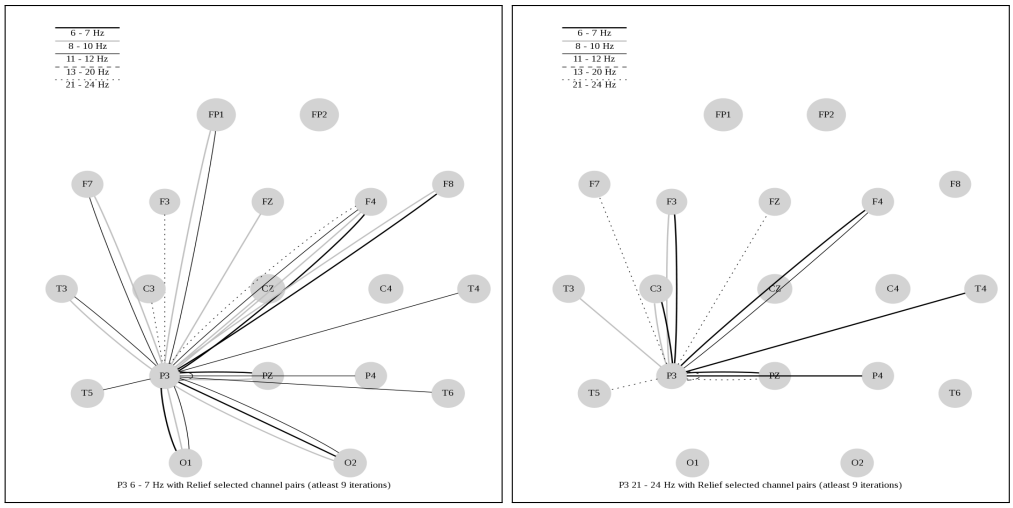

Figure 4.7: Experiment I P3 at 6-7 Hz (left) and P3 at 21-24 Hz (right)

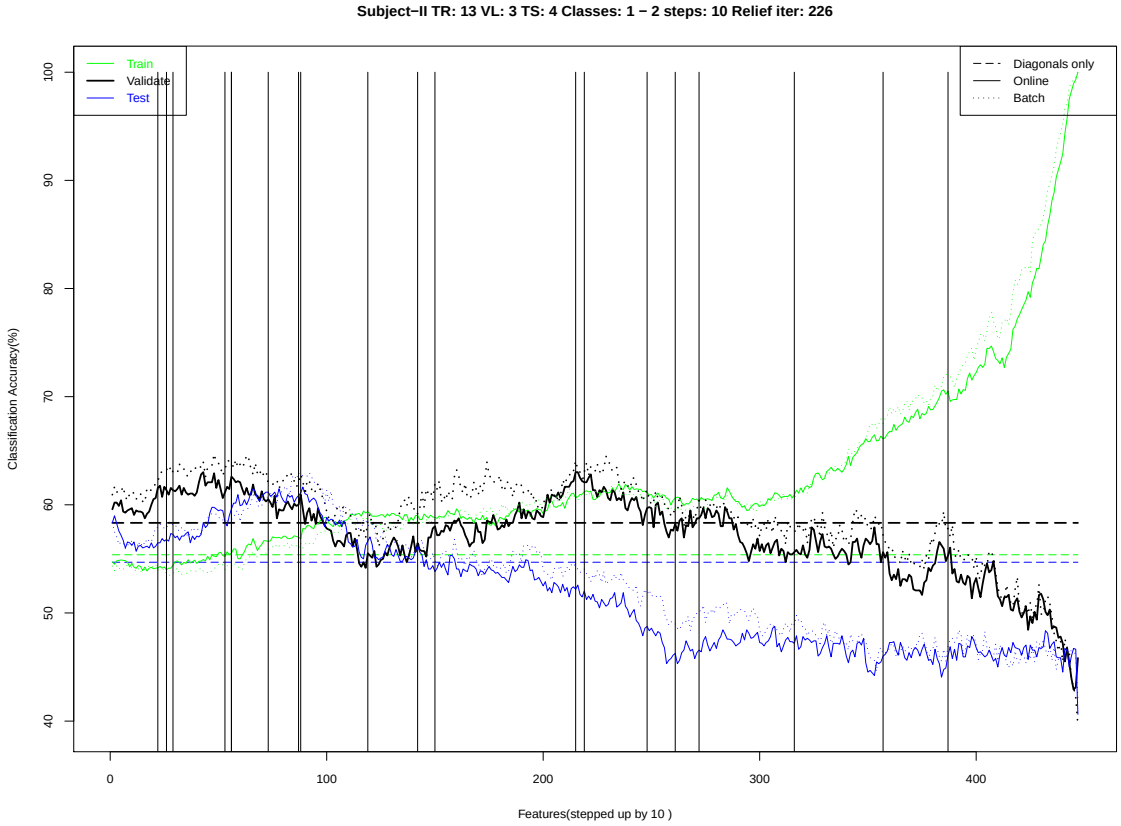

Figure 4.8: Experiment II performance plot

Table 4.2: Comparison of performances on Test partition for experiment II

	Diagonals only	**With Feature Selection**	**Without Feature Selection**
Batch QDA	56.25%	56.01%	40.62%
Incremental QDA	54.69%	56.72%	40.62%

over 20 iterations. First, over twenty iterations the peak performance of the validation set is spread non uniformly between 20 and 220 features. Additionally the validation partition peaks at two instances along the feature space which causes the peak test performances to be non uniformly spread out between these two instances. Table 4.2 shows the mean performance of the proposed BCI for experiment II over twenty iterations on the test partition. The mean test performance and standard deviation over all twenty iterations is 56.72% $\pm$ 7.41% while actual test performance (where the test partition actually peaks) is at 67.26% $\pm$ 2.23%.

We plotted the heat map for top ranked features centered on the test partition bump between 500^{th} to 1100^{th} added features. Refer to Figure 4.9. The top 10 features have several ties and include all the channels but Fp1. Observe that the test and validation partitions now follow different trends when compared to experiment I. Hence the heat map on the test bump is projecting the set of features that in a way is directly contributing to the poor performance. On the other hand the heat map of the features between 2000 and 2600 which cause a spike in the validation set is shown in Figure 4.10. We do see a lot of alpha, beta 1 and beta 2 bins ranked highly in this experiment. We speculate that if test had a similar set of features like validation then the trends would synchronize. From this heat map we probed F3 and F4 channels for possible ERS and ERD characteristics but none were clearly visible.

The reasons for poor performance of the BCI on experiment II could also be the close

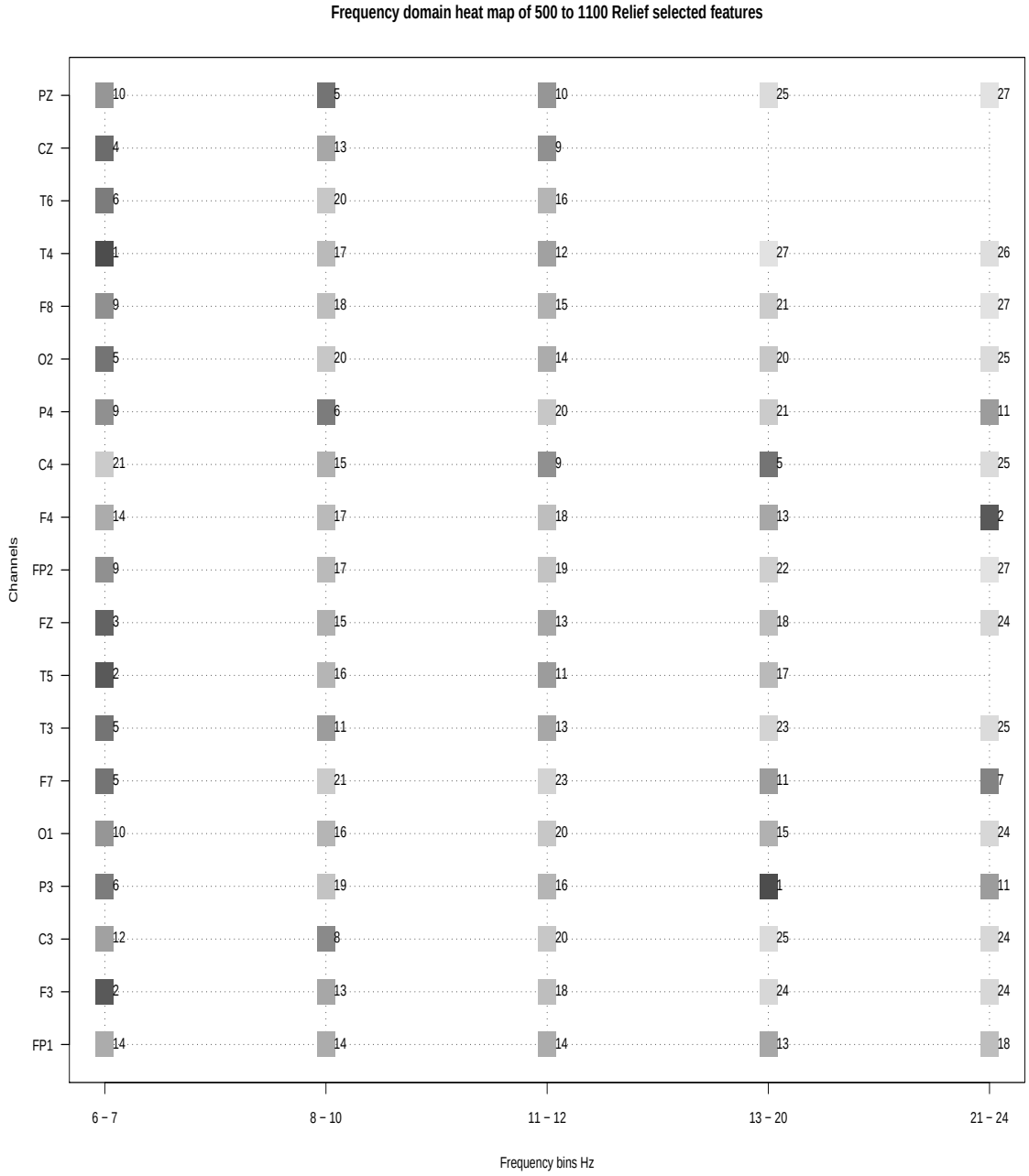

Figure 4.9: Experiment II 500 to 1100 features heat map

proximity of regions of activation in the two tasks. Additionally the cut off frequencies and grouping them into five bins may be ineffective. Also the poor performance is due

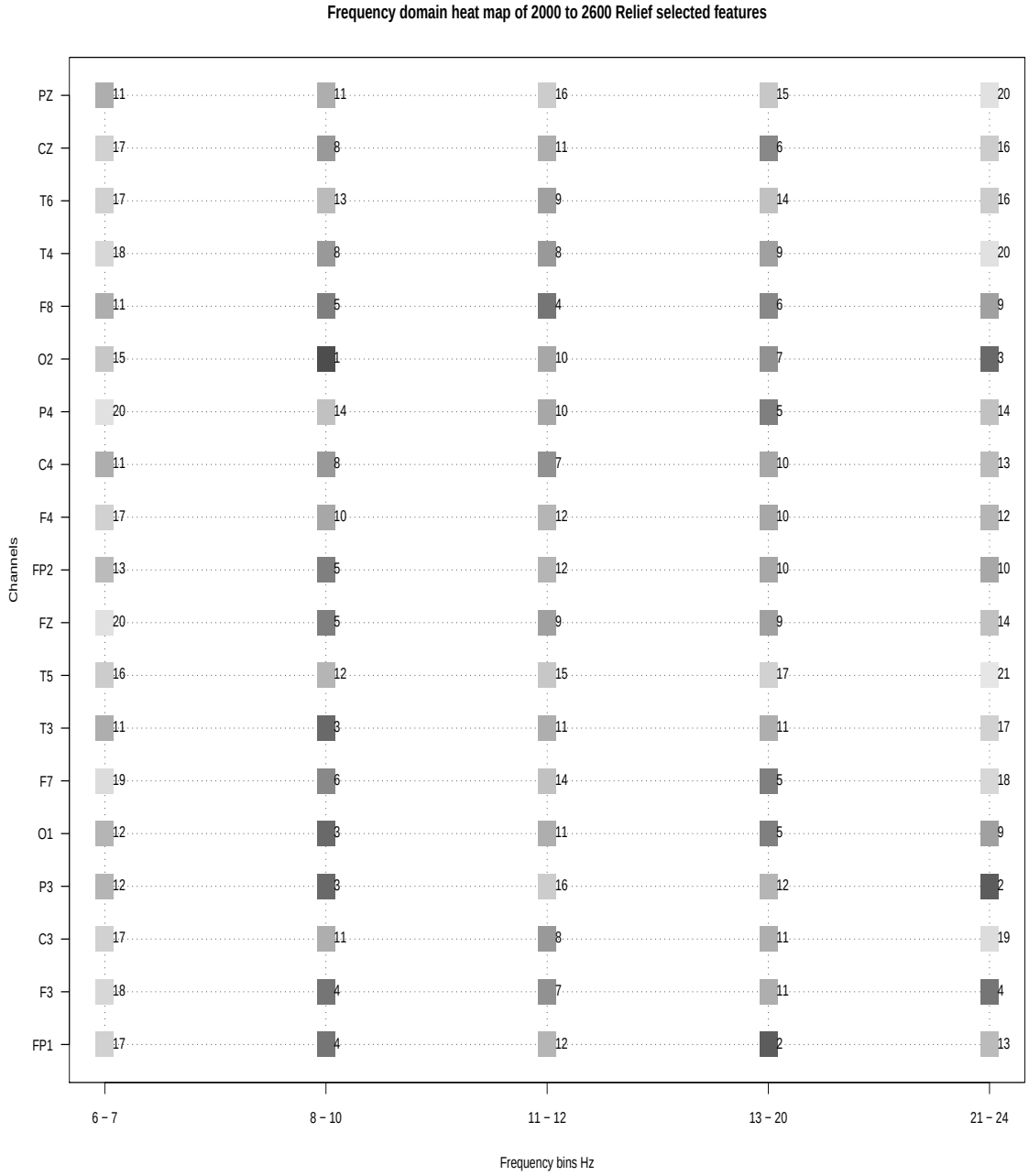

Figure 4.10: Experiment II 2000 to 2600 features heat map

to the desynchronization of the test and validation performance trends. We attribute this difference in trends between test and validation performances to be data specific par-

ticularly the partition of the train, validation and test sets. From pilot experiments, a different partition gives better performance and compatible trends but this in turn violates the time constraints placed on the partitions; from the EEG data sequences the first set of sequences goes into training, intermediate set goes into validating and the last set goes into testing, as this ordering replicates a real world problem.

4.3 Comparison of Execution Time

We compared the execution time taken to compute the inverse covariance matrix between batch, the Berge, et al., algorithm [30] and our incremental approach. In the batch approach we used the *cov()* and *solve()* [57] R functions to compute the covariance and inverse covariance, respectively. The Berge, et al., [30] algorithm is written in R and computes the inverse covariance matrix using all data samples but looping through each row in the inverse covariance matrix once and updating the corresponding columns. In essence it computes the B and D matrices similar to our incremental approach but for all samples simultaneously using matrix computations. In the incremental approach we loop over all samples and for each sample update all rows in the B and D matrices following which we compute the inverse covariance matrix. Hence for sample k from a N sample dataset such that $1 < k < N$ we have an estimated inverse covariance matrix up until the k^{th} sample. These three approaches cannot be directly compared for execution time as the first two approaches use matrix computation. Hence for the incremental approach we have plotted the average execution time over all samples. We chose to plot the average time since in an online BCI application when the inverse covariance matrix up until sample k already exists we will only need to update the inverse covariance matrix for the $k+1^{th}$ sample whereas batch and the Berge, et al., approaches will need to recompute the inverse covariance matrix for $k+1$ samples. Figure 4.11 shows the execution (elapsed) time in seconds over datasets of size 100, 1000, 10000

and 100000 samples, respectively. The number of features in each dataset is set to a constant 95 (corresponding to the number of features in our experiments). The data samples are generated from standard normal distribution. All experiments were performed on a 64 bit Linux system. It took the incremental approach approximately 163 minutes to compute the inverse covariance matrix for a 100000 sample dataset this translates to an average of 0.10 seconds per sample. Also in the incremental approach as the number of samples increased in powers of 10 (i.e. from 100 to 1000) the elapsed time increased from 21 seconds to 123 seconds. We think the real potential of this incremental approach can be explored when samples from multiple training sessions are used to only update the sparse inverse covariance matrix, as determined from the previous training session, when the other two approaches will need to compute the same using all samples from all training sessions. We realize this is not an efficient way to compare performances but nevertheless it gives some insight on the execution time of the approaches.

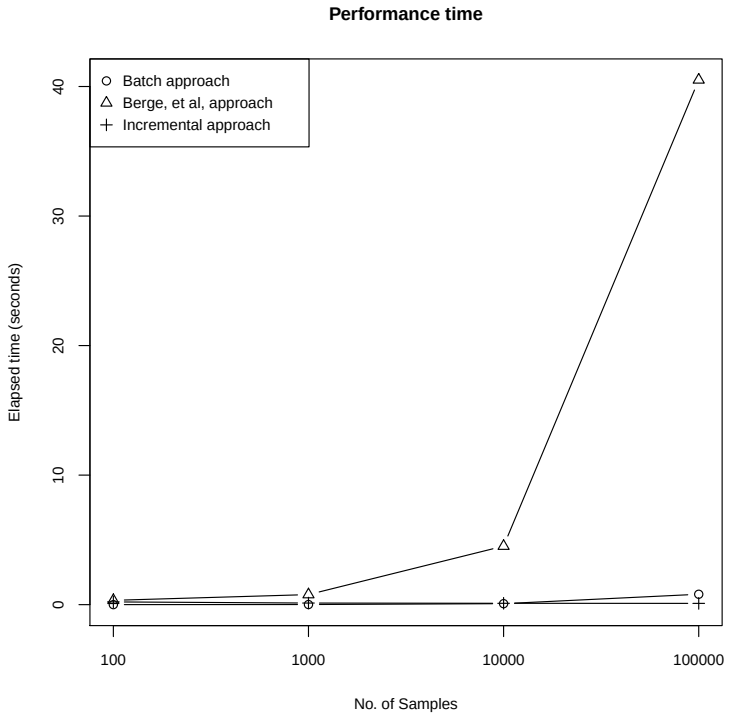

Figure 4.11: Comparison of execution time taken to compute the inverse covariance matrix

Chapter 5

Conclusion and Future Work

In this project we presented a brain-computer interface model that recognizes one task from another in a timely manner. We performed two experiments to demonstrate the strengths and weaknesses of the BCI model. Both experiments followed procedures and settings akin to real world scenarios. From the performance plots the incremental and batch approaches are compatible in performance with the added advantage that this incremental model greatly minimizes the computational complexity by updating the parameters incrementally. We performed feature selection solely to improve the recognition rates which would complement the classifier. We find that feature selection greatly improves the classification accuracies by nearly 16%. Also experiments I and II show that only 1200 of the 4465 features or a 26.87% of the total features, are required to achieve a peak performance. In terms of execution time the incremental approach takes approximately 0.13 seconds, for any given sample, to update the inverse covariance matrix. This should particularly prove useful when data samples from multiple training sessions are used to train the BCI.

From a neuroscience perspective the information provided by the selected features does not relate in obvious ways with our current understanding of the underlying brain activity. This is most likely due to the interaction between the various statistical procedures which fail to capture the big picture. Also the interaction between experimental

Table 5.1: Time Embedded lag and skip on a sample dataset

Sample dataset	**Lag 1 skip 0**	**Lag 1 skip 1**
[,1] [,2] [,3]	[,1] [,2] [,3] [,4] [,5] [,6]	[,1] [,2] [,3] [,4] [,5] [,6]
1 8.3 70 10.3	1 8.3 70 10.3 8.6 65 10.3	1 8.3 70 10.3 8.8 63 10.2
2 8.6 65 10.3	2 8.6 65 10.3 8.8 63 10.2	2 8.6 65 10.3 10.5 72 16.4
3 8.8 63 10.2	3 8.8 63 10.2 10.5 72 16.4	3 8.8 63 10.2 10.7 81 18.8
4 10.5 72 16.4	4 10.5 72 16.4 10.7 81 18.8	4 10.5 72 16.4 10.8 83 19.7
5 10.7 81 18.8	5 10.7 81 18.8 10.8 83 19.7	5 10.7 81 18.8 11.0 66 15.6
6 10.8 83 19.7	6 10.8 83 19.7 11.0 66 15.6	6 10.8 83 19.7 11.0 75 18.2
7 11.0 66 15.6	7 11.0 66 15.6 11.0 75 18.2	7 11.0 66 15.6 11.1 80 22.6
8 11.0 75 18.2	8 11.0 75 18.2 11.1 80 22.6	8 11.0 75 18.2 11.2 75 19.9
9 11.1 80 22.6	9 11.1 80 22.6 11.2 75 19.9	
10 11.2 75 19.9		

settings have not been systematically explored in this project. This includes parameters from power spectral density estimation: window size, window type, individual PSDs versus averaged PSDs, cut off frequencies and grouping of frequencies into bins; from Relief the number of iterations. We believe these settings will need to be probed per subject and/or per task basis and should not be generalized.

One direction of future work is the investigation of EEG signals in the time domain (i.e., by not estimating the power spectral densities instead using the raw EEG data to recognize tasks) with and without time embedded lag. In the time domain the incremental QDA's performance is consistent with batch QDA. But it appears that in both approaches the top features as ranked by Relief fail to improve performance. As a result the BCI's performance is close to and in some cases worse then random performance. We would like to study in detail the reasons for this poor performance. Within time domain, time embedded lag uses multiple samples to make a classification decision. A skip factor determines how many samples are interleaved to make a decision. When

skip is zero the samples are adjacent. Refer to Table 5.1 for a time embedded lag and skip example on a ten sample three attribute dataset. It has been demonstrated that time embedded lag considerably improves recognition rates in EEG based brain-computer interface [58]. We performed some preliminary experiments with time embedded lag with and without skip on the dataset I. It was identified that for right hand and visual spinning tasks the best lag skip combination is 5-5. Using this lag-skip combination on the validation set results in a recognition rate of 75.33% without any feature selection. Another subject for future work would be a more systematic approach to determine the cut off frequencies and grouping of frequencies into bins in frequency domain. We would also like to experiment with more datasets to check for consistency in trends and performance.

REFERENCES

[1] J. R. Wolpaw, N. Birbaumer, W. J. Heetderks, D. J. McFarland, P. H. Peckham, G. Schalk, E. Donchin, L. A. Quatrano, C. J. Robinson, and T. M. Vaughan. Brain Computer Interface Technology: A Review of the First International Meeting. *IEEE Transactions on Rehabilitation Engineering*, 8(2):164–173, 2000.

[2] J. N. Knight. Signal Fraction Analysis and Artifact Removal in EEG. Master's thesis, Colorado State University, Fort Collins, CO, 2003.

[3] D. J. McFarland, W. A. Sarnacki, T. M. Vaughan, and J. R. Wolpaw. Brain-computer interface (BCI) operation: signal and noise during early training sessions. *Clinical Neurophysiology*, 116(1):56–62, 2005.

[4] A. Kübler, F. Nijboer, J. Mellinger, T. M. Vaughan, H. Pawelzik, G. Schalk, D. J. McFarland, N. Birbaumer, and J. R. Wolpaw. Patients with ALS can use sensorimotor rhythms to operate a brain-computer interface. *Neurology*, 64(10):1775–1777, 2005.

[5] J. del R. Millán, J. Mouri no, M. Franzé, F. Cincotti, M. Varsta, J. Heikkonen, and F. Babiloni. A Local Neural Classifier for the Recognition of EEG Patterns Associated to Mental Tasks. *IEEE Transactions on Neural Networks*, 13(3):678–686, 2002.

[6] A. J. Murias. Biology and Geology Interaction in Humans. `http://www.sciencehelpdesk.com`.

[7] M. Teplan. Fundamentals of EEG Measurement. *Measurement Science Review*, 2:1–11, 2002.

[8] R. M. Stern, W. J. Ray, and K. S. Quigley. Brain Electroencephalography and Imaging. In *Psychophysiological Recording*, pages 79–105. Oxford University Press, 2000.

[9] J. del R. Millán, P.W. Ferrez, F. Galán, E. Lew, and R. Chavarriaga. Non Invasive Brain-Machine Interaction. *International Journal of Pattern Recognition and Artificial Intelligence*, 20(10):1–13, 2007.

[10] Wikipedia. Electroencephalography. http://en.wikipedia.org/wiki/Electroencephalography.

[11] S. Sanei and J. A. Chambers. *EEG Signal Processing*. Wiley-Interscience, 2007.

[12] O. Jensen, J. Kaiser, and J. P. Lachaux. Human gamma-frequency oscillations associated with attention and memory. *Trends in Neurosciences*, 30(7):317–324, 2007.

[13] J. del R. Millán and P.W. Ferrez. Error-related EEG potentials generated during simulated brain-computer interaction. *IEEE Transactions on Biomedical Engineering*, 55(3):923–929, 2008.

[14] G. V. Kondraske. Neurophysiological Measurements. In J. Bronzino, editor, *Biomedical Engineering and Instrumentation: Basic Concepts and Applications*, pages 138–179. PWS Engineering, 1986.

[15] NeuroPulse Systems. Neuropulse Systems LLC. http://www.np-systems.com/.

[16] E. H. Chudler. Neuroscience for Kids. http://faculty.washington.edu/chudler/1020.html.

[17] C. Anderson. CSU EEG Brain-computer interface Lab (CEBL). http://www.cs.colostate.edu/eeg/eegSoftware.html.

[18] F. Galán, M. Nuttin, E. Lew, P.W. Ferrez, G. Vanacker, J. Philips, and J. del R. Millán. A brain-actuated wheelchair: asynchronous and non-invasive brain-computer interfaces for continuous control of robots. *Clinical Neurophysiology*, 119(9):2159–2169, 2008.

[19] K. Tanaka, T. Kurita, F. Meyer, L. Berthouze, and T. Kawabe. Stepwise Feature Selection by Cross Validation for EEG-based brain computer Interface. In *2006 International Joint Conference on Neural Networks*, pages 4672–4677, 2006.

[20] A. Y. Kaplan, A. A. Fingelkurts, A. A. Fingelkurts, S. V. Borisov, and B. S. Darkhovsky. Nonstationary nature of the brain activity as revealed by EEG/MEG: Methodological, practical and conceptual challenges. *Signal Processing*, 85(11):2190–2212, 2005.

[21] N. Srinivasan. Cognitive neuroscience of creativity: EEG based approaches. *Neurocognitive Mechanisms of Creativity: A Toolkit, Methods*, 42(2):109–116, 2007.

[22] G. Pfurtscheller, P. Linortner, R. Winkler, G. Korisek, and G. Müller-Putz. Discrimination of Motor Imagery-Induced EEG Patterns in Patients with Complete Spinal Cord Injury. *Computational Intelligence and Neuroscience*, 2009:published online, 2009.

[23] W.Tao, D. Jie, and H. Bin. Classification of motor imagery EEG patterns and their topographic representation. In *Annual International Conference of the IEEE Engineering in Medicine and Biology Society*, volume 2, pages 4359–4362, 2004.

[24] G. Pfurtscheller, C. Neuper, A. Schlögl, and K. Lugger. Separability of EEG signals recorded during right and left motor imagery using adaptive autoregressive parameters. *IEEE Transactions on Rehabilitation Engineering*, 6(3):316–325, 1998.

[25] D. J. McFarland, L. McCane, L. A. Miner, T. M. Vaughan, and J. R. Wolpaw. EEG mu and beta rhythm topographies with movement imagery and actual movement. *Society for Neuroscience Abstracts*, page 1277, 1997.

[26] J. R. Wolpaw, D. J. McFarland, G. W. Neat, and C. A. Forneris. An EEG-Based Brain Computer Interface for Cursor Control. *Electroencephalography and clinical neurophysiology*, 78(3):252–259, 1991.

[27] B. Rescher and P. Rappelsberger. Gender dependent EEG-changes during a mental rotation task. *International Journal of Psychophysiology*, 33(3):209–222, 1999.

[28] E. Dimitriadou, K. Hornik, F. Leisch, D. Meyer, and A. Weingessel. R package e1071. `http://cran.r-project.org/web/packages/e1071/index.html`.

[29] C. M. Bishop. *Pattern Recognition and Machine Learning*. Springer, 2007.

[30] A. Berge, A. Jensen, and A. S. Solberg. Sparse Inverse Covariance Estimates for Hyperspectral Image Classification. *IEEE Transactions on Geoscience and Remote Sensing*, 45(5):1399–1407, 2007.

[31] W. D. Penny. Kullback-Leibler Divergences of Normal, Gamma, Dirichlet and Wishart densities. `http://www.fil.ion.ucl.ac.uk/~wpenny/publications/densities.ps`.

[32] P. Simecek. R Package yest. `http://cran.r-project.org/web/packages/yest/index.html`.

[33] I. Guyon and A. Elisseeff. An Introduction to Feature Extraction. In I. Guyon, S. Gunn, M. Nikravesh, and L. A. Zadeh, editors, *Feature Extraction Foundations and Applications, Series: Studies in Fuzziness and Soft Computing*, pages 1–25. Springer, 2006.

[34] M. Robnik-Šikonja and I. Kononenko. Theoretical and Empirical Analysis of ReliefF and RreliefF. *Machine Learning*, 53(1-2):23–69, 2003.

[35] A. Guillot, C. Collet, V. A. Nguyen, F. Malouin, C. Richards, and J. Doyon. Brain activity during visual versus kinesthetic imagery: an fMRI study. *Human Brain Mapping*, 30(7):2157–2172, 2009.

[36] G. Ganis, W. L. Thompson, F. Mast, and S. M. Kossyln. The Brains Minds images: The Cognitive Neuroscience of Mental Imagery. In M. S. Gazzaniga, editor, *The Cognitive Neurosciences*, pages 931–941. The MIT Press, 2004.

[37] S. Lehéricy, E. Gerardin, J. B. Poline, S. Meunier, P. F. Van de Moortele, D. Le Bihan, and M. Vidailhet. Motor execution and imagination networks in post-stroke dystonia. *Neuroreport*, 15(12):1887–1890, 2004.

[38] E. Gerardin, A. Sirigu, S. Lehéricy, J. B. Poline, B. Gaymard, C. Marsault, Y. Agid, and D Le Bihan. Partially overlapping neural networks for real and imagined hand movements. *Cerebral Cortex*, 10(11):1093–1104, 2000.

[39] G. Pfurtscheller and C. Neuper. Motor imagery activates primary sensorimotor area in humans. *Neuroscience Letters*, 239(2-3):65–68, 1997.

[40] C. M. Stinear, W. D. Byblow, M. Steyvers, O. Levin, and S. P. Swinnen. Kinesthetic, but not visual, motor imagery modulates corticomotor excitability. *Experimental Brain Research*, 168(1-2):157–164, 2006.

[41] J. L. Andreassi. *Psychophysiology: Human Behavior and Physiological Response*. Lawrence Erlbaum, 2000.

[42] G. Ganis, W. L. Thompson, and S. M. Kosslyn. Brain areas underlying visual mental imagery and visual perception:an fMRI study. *Cognitive Brain Research*, 20(2):226–241, 2004.

[43] S. M. Kosslyn, W. L. Thompson, and G. Ganis. *The Case for Mental Imagery*. Oxford University Press, 2006.

[44] A. R. Nikolaev and A.P. Anokhin. EEG frequency ranges during perception and mental rotation of two-and three-dimensional objects. *Biomedical and Life Sciences*, 28(6):670–677, 1998.

[45] M. Wexler, S. M. Kosslyn, and A. Berthoz. Motor processes in mental rotation. *Cognition*, 68(1):77–94, 1998.

[46] S. H. Choi and M. Lee. Estimation of Motor Imaginary using fMRI Experiment based EEG Sensor Location. *International Journal of Computational Intelligence Research*, 3(1):46–49, 2007.

[47] G. Pfurtscheller and F. L. da Silva. EEG Event-Related Desynchronization (ERD) and Event-Related Synchronization (ERS). In E. Niedermeyer and F. L. da Silva, editors, *Electroencephalography: Basic Principles, Clinical Applications, and Related Fields*, pages 1003–1016. Lippincott Williams & Wilkins, 2004.

[48] G. Pfurtscheller, R. Scherer, and C. Neuper. EEG-based Brain Computer Interface. In R. Parasuraman and M. Rizzo, editors, *Neuroergonomics: The Brain at Work (Oxford Series in Human-Technology Interaction)*, pages 315–328. Oxford University Press, 2006.

[49] G. Pfurtscheller and C. Neuper. Motor Imagery activates primary sensorimotor area in humans. *Neuroscience Letters*, 239(2-3):65–68, 1997.

[50] L. Qin, L. Ding, and Bin He. Motor imagery classification by means of source analysis for brain computer interface applications. *Journal of Neural Engineering*, 1(3):135–141, 2004.

[51] R. Beisteiner, P. Höllinger, G. Lindinger, W. Lang, and A. Berthoz. Mental representations of movements. Brain potentials associated with imagination of hand movements. *Electroencephalography and Clinical Neurophysiology*, 96(6):183–193, 1995.

[52] H. Ramoser, J. M. Gerking, and G. Pfurtscheller. Optimal Spatial Filtering of Single Trial EEG During Imagined Hand Movement. *IEEE Transactions on Rehabilitation Engineering*, 8(4):441–446, 2000.

[53] B. Kamousi, Z. Liu, and B. He. An EEG Inverse Solution based Brain-Computer Interface. *International Society for Bioelectromagnetism*, 7(2):Online journal, 2005.

[54] D. Popivanov, S. Jivkova, V. Stomonyakov, and G. Nicolova. Effect of independent component analysis on multifractality of EEG during visual-motor task. *Signal Processing*, 85(11):2112–2123, 2005.

[55] A. Erfani and A. Erfanian. The Effects of Mental practice and Concentration Skills on EEG Brain Dynamics During Motor Imagery Using Independent Component Analysis. In *26th Annual International Conference of the IEEE EMBS*, volume 1, pages 239–242, 2004.

[56] F. Malouin, S. Belleville, C. L. Richards, J. Desrosiers, and J. Doyon. Working memory and mental practice outcomes after stroke. *Archives of Physical Medicine and Rehabilitation*, 85(2):177–183, 2005.

[57] R. A. Becker, J. M. Chambers, and A. R. Wilks. *The New S Language: A Programming Environment for Data Analysis and Graphics*. Chapman & Hall, 1988.

[58] A. Sokolov. Analysis of Temporal Structure and Normality in EEG data. Master's thesis, Colorado State University, Fort Collins, CO, 2007.